NASA TECHNICAL NOTE

NASA TN D-6672

NASA TN D-6672

PRACTICAL CONSIDERATIONS FOR ABEL INVERTING OF PHOTOGRAPHIC DATA WITH APPLICATION TO THE ANALYSIS OF A 15-kW WALL-STABILIZED ARC-LIGHT SOURCE

by Walter L. Snow

Langley Research Center
Hampton, Va. 23365

NATIONAL AERONAUTICS AND SPACE ADMINISTRATION • WASHINGTON, D. C. • MARCH 1972

1. Report No. NASA TN D-6672	2. Government Accession No.	3. Recipient's Catalog No.

4. Title and Subtitle PRACTICAL CONSIDERATIONS FOR ABEL INVERTING OF PHOTOGRAPHIC DATA WITH APPLICATION TO THE ANALYSIS OF A 15-kW WALL-STABILIZED ARC-LIGHT SOURCE	5. Report Date March 1972 6. Performing Organization Code
7. Author(s) Walter L. Snow	8. Performing Organization Report No. L-8071
9. Performing Organization Name and Address NASA Langley Research Center Hampton, Va. 23365	10. Work Unit No. 117-07-04-04 11. Contract or Grant No.
12. Sponsoring Agency Name and Address National Aeronautics and Space Administration Washington, D.C. 20546	13. Type of Report and Period Covered Technical Note 14. Sponsoring Agency Code

15. Supplementary Notes

16. Abstract

Temperature profiles were measured for argon at atmospheric pressure by using absolute line and continuum intensity and were compared with Stark width and shift measurements. A detailed analysis of the engineering aspects of setting up for Abel inverting data photographically is presented. The merits of using photographic detection and of using continuum radiation for temperature profile analysis are discussed. The importance of empirically determining the optical depth is emphasized by discrepancies between measured (two-path) and calculated estimates.

17. Key Words (Suggested by Author(s)) Abel inversion Photographic inversion Stabilized arc	18. Distribution Statement Unclassified – Unlimited

19. Security Classif. (of this report) Unclassified	20. Security Classif. (of this page) Unclassified	21. No. of Pages 56	22. Price* $3.00

*For sale by the National Technical Information Service, Springfield, Virginia 22151

PRACTICAL CONSIDERATIONS FOR ABEL INVERTING OF PHOTOGRAPHIC DATA WITH APPLICATION TO THE ANALYSIS OF A 15-kW WALL-STABILIZED ARC-LIGHT SOURCE

By Walter L. Snow
Langley Research Center

SUMMARY

A wall-stabilized arc source is used to study the practical aspects of photographic Abel inversion. The convergence-free problem is set up in terms of energy variables and in the limit, the Abel transform derived as it applies to the spectroscopic problem. The detailed inversion of the transform makes explicit the implied boundary conditions in the solution and also displays two alternative forms to which numerical analysis is usually applied.

The stop is identified which determines the spatial resolution in both photoelectric and photographic modes. An expression for the effective spatial resolution is derived in terms of the aperture and field stops of the system with due attention to depth of field and optical resolution. An upper bound for the relative volume error incurred because of converging optics is obtained in terms of geometrical dimensions of the system.

Temperature profiles were derived from absolute intensity measurements of continuum and atomic line radiation. Measurements relate to atmospheric pressure argon with maximum flow rate of 3×10^{-5} m^3/sec (4 ft^3/hr) at root-mean-square power levels between 2 and 15 kW. Equilibrium plasma at 8000 K to 12 000 K was generated under these conditions. Theoretical and experimental estimates of optical depth for 4300 ArI are contrasted. Stark width and shift data for 4300 ArI were used as self-consistency checks for the axial temperatures derived from "side on" measurements.

INTRODUCTION

The popularity of Abel inversion for analysis of cylindrically symmetric phenomena is evidenced by the number of references to it in recent spectroscopic literature. Unfortunately, for one reason or another, the practical aspects can only be gleaned with difficulty by anyone interested in his own possible application. This statement is especially true for the photographic-detection mode. This note will attempt to elaborate on the method and its limitations.

The usefulness of wall-stabilized or cascade arcs as plasma light sources is well established. (For example, see ref. 1 (p. 205) and references therein.) Local thermodynamic equilibrium (LTE) and cylindrically symmetric geometry allow chordal observations to be interpreted in terms of radial temperature profiles. Such an arc serves in this study as a convenient tool for studying the experimental aspects of Abel inversion. The working gas was atmospheric pressure argon and consequently, the temperature profiles reported simply corroborate an existing bank of published data. (See refs. 2 to 5.)

Several features distinguish this treatment from others. Instead of taking the Abel transform description as a starting point, as is usually done, it is developed here from basic considerations as the limit of a sum, and its solution is explicitly carried through to underscore boundary conditions entering into the problem. The two alternative forms to which numerical analysis is often applied are shown.

The physical stops which limit spatial resolution are identified with due regard to their effects on depth of field and optical resolution. An approximate expression for the relative volume error incurred because of the use of converging optics is derived and is helpful in assessing alternative experimental schemes.

Development of the Abel transform from a volume-weighted sum as is done here clarifies the optical thin assumption underlying the end result. The danger of relying too much on theoretical assurances of optical thinness is demonstrated by contrasting theoretical and experimental estimates of the peak absorption for the 4300 ArI line.

SYMBOLS

A	area, cm^2; also mass, atomic mass units
$A_{u \to l}$	transition probability, sec^{-1}
a	line shape parameter, dimensionless, $\frac{w_{col}}{w_{Dop}}\sqrt{\log_e 2}$
B_{Str}	brightness or steradiancy, used interchangeably with specific intensity. It is defined as the power per steradian per projected area of source in the direction of the detector, W(cm^2-sr)$^{-1}$. When subscripted with λ it is a per spectral interval quantity having units W(cm^2-sr-Å)$^{-1}$.
$\bar{B}$	functional form of steradiancy in terms of β having units of B_{Str}
C	empirical correction factor for intensity, dimensionless

D	optical density defined as minus the common logarithm of the transmission of a photographic negative or aperture diameter, mm
d	Stark shift, angstroms
E	energy level, cm^{-1}
F	focal length, cm
f	oscillator strength, dimensionless
f( )	dummy function
g	apparatus function, $angstrom^{-1}$, or statistical weight, dimensionless
H	slit height (that is, dimension perpendicular to direction of scan), mm
h	sagitta, cm; also Planck's constant, 6.623×10^{-34} joule-sec
I	specific intensity, $W(cm^2\text{-}sr)^{-1}$
K	proportionality constant (deflection of densitometer pen per unit exposure on film), $mm\text{-}erg^{-1}$ (10^7 ergs = 1 joule)
k	linear absorption coefficient, cm^{-1}
$\mathcal{L}$	line shape, $angstrom^{-1}$
m	lateral magnification, dimensionless
N	number density, cm^{-3}
n	number of zones, dimensionless
p	dummy variable, cm^2
R	radius at which arc ceases to emit detectable radiation, mm
$\mathcal{R}$	reflectivity, dimensionless

r	polar radial coordinate, cm
r_e	classical radius of electron, 2.8179×10^{-13} cm
S	lens to arc distance, cm; also integrated absorption, dimensionless for wavelength-related case
S_{sig}	signal deflection, mm
s	geometric optics distance, cm
T	temperature, K
t	time, sec
u,v	dummy variables for integration by parts
V	volume, cm^{-3}
W	slit width (that is, dimension along scan direction), mm
w	line width at half peak, angstroms
w	dimensionless slit width
Z	partition function, dimensionless
α	scaling factor for polar radial coordinate, cm^2
β	scaling factor for Cartesian coordinate, cm^2
β_{ij}	ij^{th} element of Abel inversion matrix, dimensionless
Δ	depth of field, cm, or zone width for inversion, cm; also used as a small difference
$\Delta x, \Delta y, \Delta z$	small increments of Cartesian coordinates x, y, and z, cm
δ	depth of focus, cm

$\delta(x)$	Dirac delta function
ϵ	volume emission coefficient, $W(cm^3\text{-}sr)^{-1}$; also minimum resolvable dimension on film, mm, or emissivity, dimensionless
$\bar{\epsilon}$	functional form of the volume emission coefficient when written in terms of α, $W(cm^3\text{-}sr)^{-1}$
ν	frequency, sec^{-1}
Ω	solid angle, sr
τ	transmission, dimensionless
θ	angle defined in figure 11, radians
ξ	Guant factor, dimensionless

Subscripts:

B	brightness
b	back, that is, side furthest from detector
c	collecting
col	collision
d	densitometer
Dop	Doppler
e	electron
eff	effective
f	front, that is, side nearest detector
l	lower level

o	line center
max	maximum
pyr	pyrometer
s	slit
t	true
u	upper level
λ	wavelength, a spectral quantity
□	rectangular

Superscripts:

(arc)	arc
cont	continuum
L	line
meas	measured
nd	neutral density
o	black body
obs	observed
opt	optics
pl	plasma
thin	optically thin
(W)	tungsten

' image space quantity

+ ion

DESCRIPTION OF THE ARC LIGHT SOURCE AND ITS OPERATION

The light source is patterned after the design of Shumaker (ref. 6). The arc is maintained between two cylindrical tungsten electrodes which serve as cathode and anode and is constrained by a stack of annular, water-cooled segments, each having a central bore of 6 mm. The segments are separated from each other by the ring windows used for viewing and from the arc housing by dielectric spacers. The interelectrode spacing is fixed at 7.6 cm.

The arc unit is pictured in figure 1(a) and a schematic labeling of the main components is shown in figure 1(b). The control center for the arc is shown in figure 2(a) and the flexibility of the gas porting system is suggested in figure 2(b). The option of exhausting into a manifold which is vacuum pumped allows the system to operate at total pressures down to 6000 newtons per meter^2 (0.06 atmosphere).

Electrical power is supplied by three arc welder units suitably filtered. For the source to be adequately described by a constant-temperature profile, good filtering is essential since the current density which controls it varies linearly with current in a wall-stabilized arc. Figure 3 shows the electrical schematic. Bus-bar arrangements allow machines to be connected with or without a water-cooled load resistor to yield a current range of 30 to 150 amperes in argon. The operating limit is set by total voltage available from the supplies. Considerably higher currents could be achieved by shortening the arc column. Figure 4 depicts the arc characteristic curve. Total arc voltage was determined by measuring the field gradient between consecutive disks and multiplying by the electrode separation to guard against changes in the anode and cathode fall regions which can occur when increased current heats the electrode. (See ref. 7, p. 29.)

To strike the arc, an end window is removed and voltage is applied to the electrodes. The operator deftly inserts and withdraws a carbon rod, touching the rear electrode, and subsequently draws the arc which is formed through to the near electrode. The arc usually spins around the cylindrical electrodes for several minutes and finally attaches to one spot and remains quiescent for hours thereafter.

The arc runs best in pure argon as has been noted by previous investigators. The temperature dependence of its electrical and thermal conductivity is apparently well suited to the dimensions and current ranges of this experiment. In contrast, when helium or nitrogen is used in the arc, it becomes quite unstable and eventually attaches to one of the segments, and the run must be terminated to prevent cooling failure. Others have

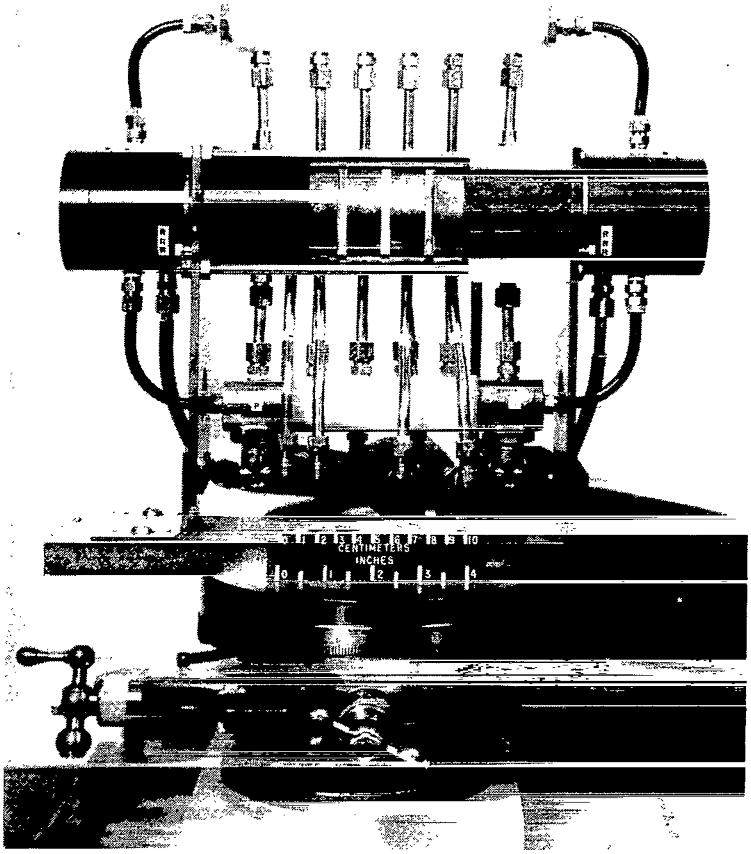

L-71-5865

(a) Side view of arc housing.

Figure 1.- Stabilized arc.

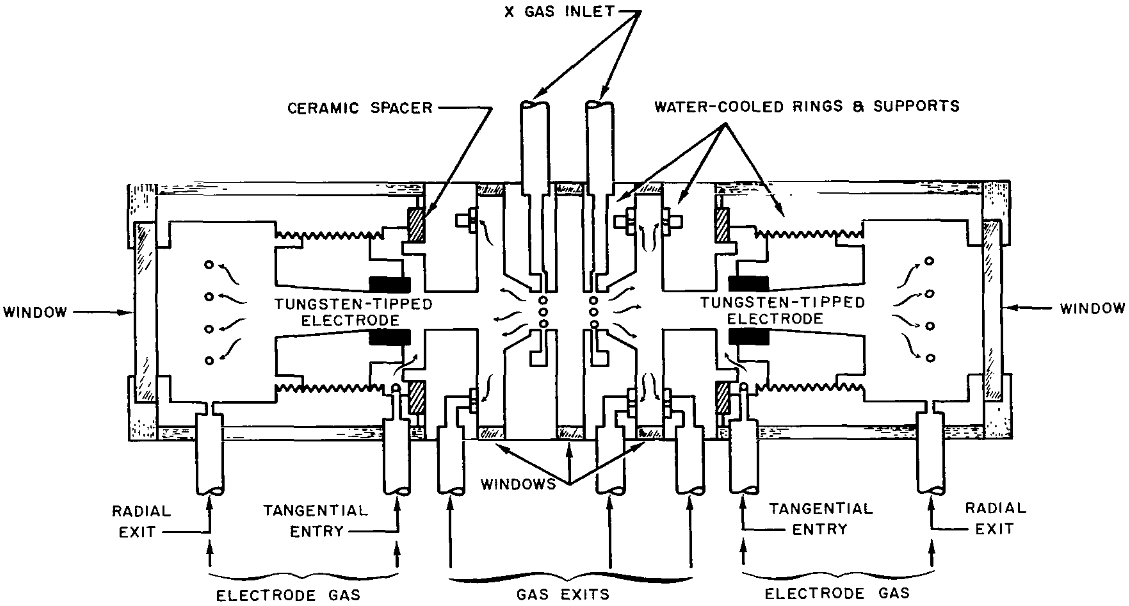

(b) Schematic showing gas, cooling, and viewing arrangements.

Figure 1.- Concluded.

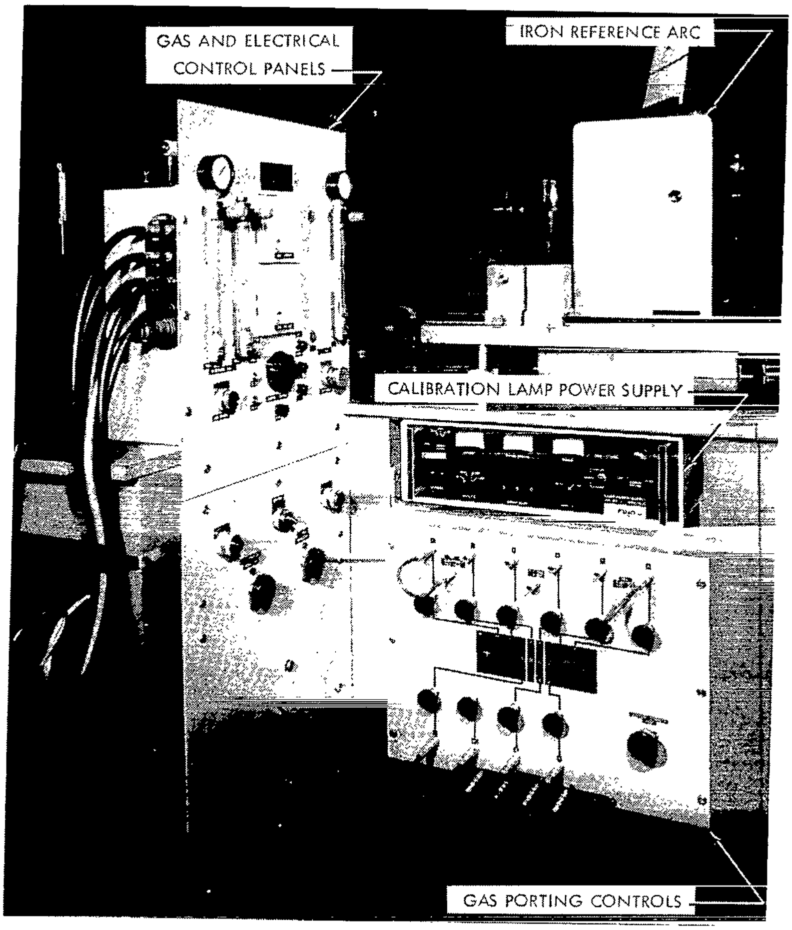

L-71-5862

(a) Current and gas flow controls.

Figure 2.- Control center for the arc.

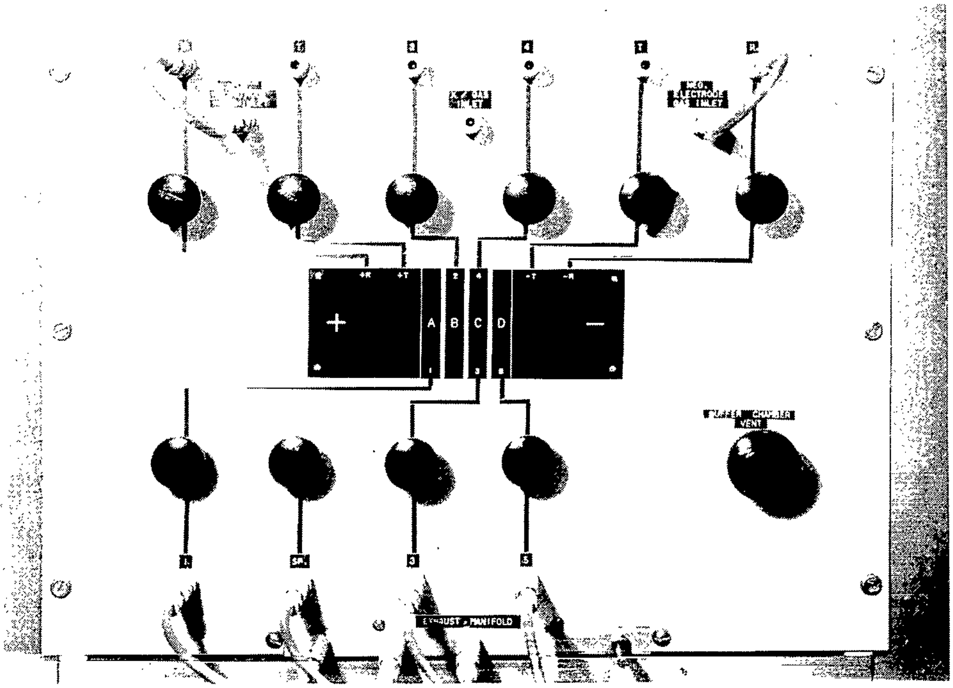

L-71-5863

(b) Gas porting panel.

Figure 2.- Concluded.

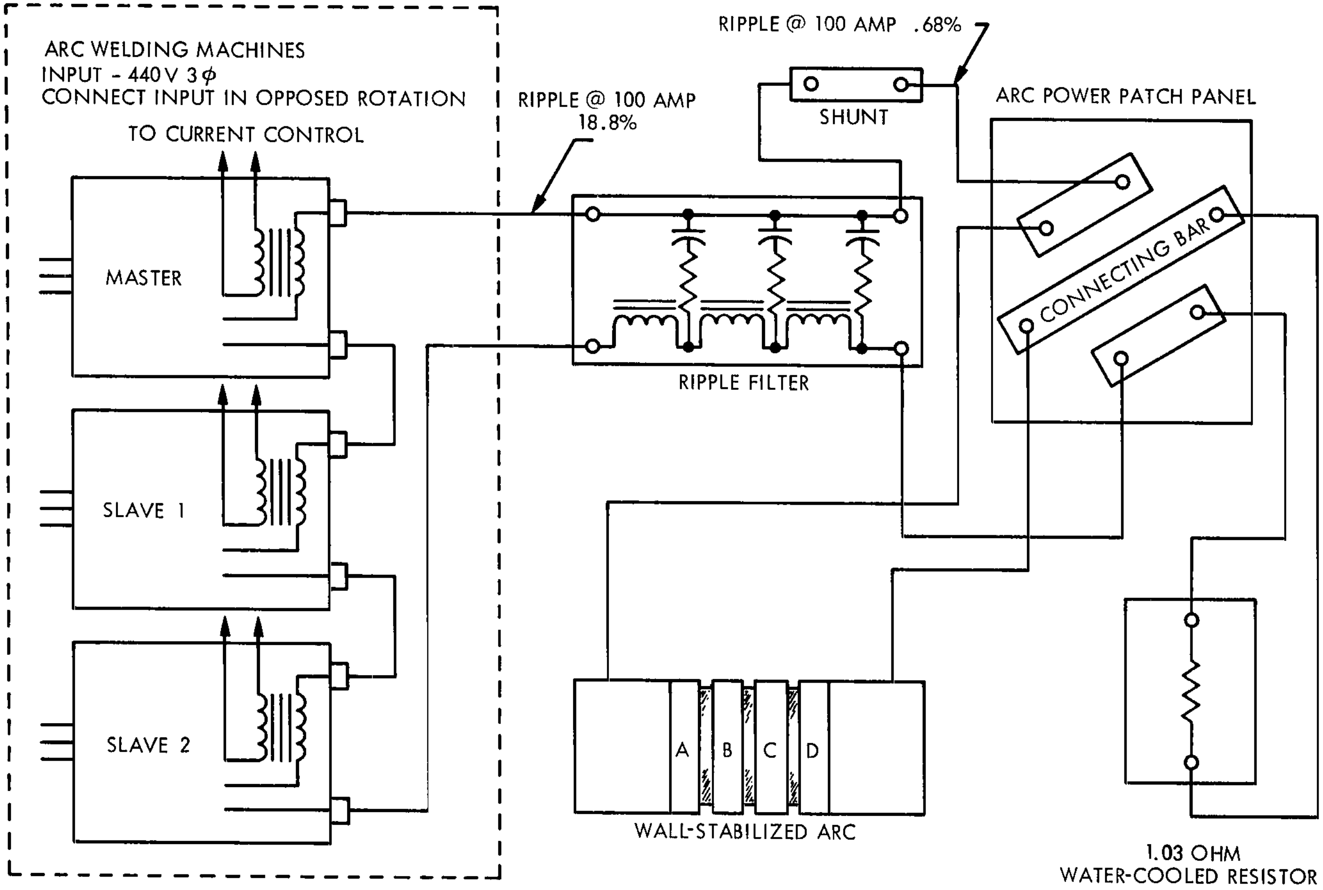

Figure 3.- Electrical layout used to filter and extend operating range of arc.

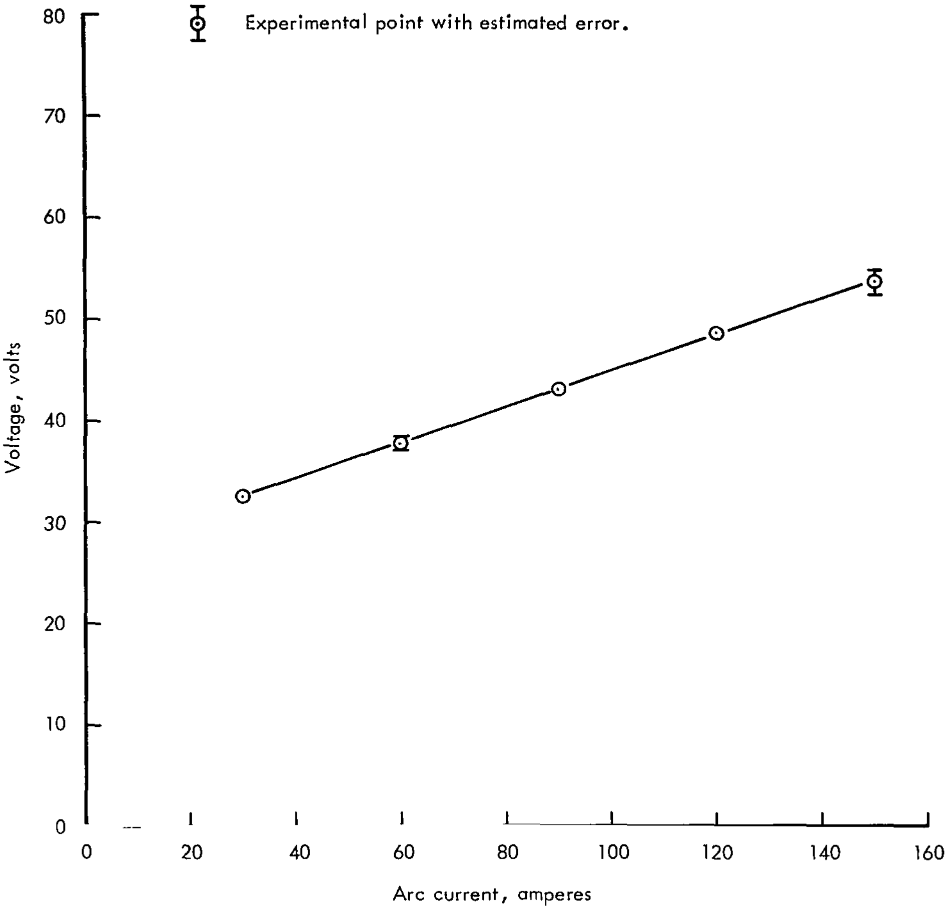

Figure 4.- Characteristic curve of the 7.6-cm arc run in atmospheric argon.

experienced similar problems with hydrogen (ref. 8). To use this arc in such gases, it is usually advisable to isolate the test gas in the center section and use the argon to blanket the electrodes as suggested by Shumaker (ref. 6). The porting arrangement was designed with this procedure in mind. Because of the low flow rates used in this work, the arc is not well suited for introducing nongaseous contaminants. Attempts to introduce copper by placing a copper rod on one of the electrodes was unsuccessful. The blue-green radiation characteristic of copper could be seen next to the electrode, but evidently the copper plated out long before entering the test region since no trace of copper was detected spectroscopically.

Since this configuration is a wall-stabilized configuration, it is natural that the arc will tend to bulge out into the viewing ports. The windows are 5 mm wide and the bulging is very noticeable, especially at high currents. The bulging often does not occur symmetrically but will develop peculiar kinks because of some unknown combination of flow rates and field gradients. Any deviation from cylindrical symmetry negates the Abel inversion concept. Asymmetry can usually be detected a posteriori by folding the densitometered data about its center line to look for features on one side that do not appear on the other. To illustrate the effect, figure 5 was prepared from an isodensity trace of a plate taken in the slitless mode of a 3.4-meter Ebert spectrograph. The instrument aperture ratio is f/33; the instrument has a plate factor of 5 Å/mm and 0.04 Å resolution in the first order by use of a 590-groove/mm grating. (10 Å = 1 nanometer.) The arc was viewed from the side so that the viewing port itself acted as the slit. The figure is interpreted in the following manner: The clear area represents background density on the plate. When the density increases by a predetermined ΔD, the plotting code changes in the order blank, dot, dash, blank, etc.; the order reverses if the increment is negative. Figure 5(a) shows a case which was judged visually to be symmetric and figure 5(b), one which was obviously distorted.

Narrower windows, shorter arc column, and smaller bore should improve the performance of the facility with the harder-to-run gases and lessen the bulging problem in all cases.

MEASUREMENT OF RADIAL EMISSION COEFFICIENT

In an arc where the electric field defines a direction in space and many processes are governed by diffusion, there is a natural tendency for axial symmetry. This natural tendency is enhanced by the boundary conditions in the wall-stabilized or cascade arc. In this situation, it is assumed that the physical parameters characterizing the phenomenon (for example, emission coefficients, particle densities, temperatures, etc.) are functions of the radius r only. This dependence can be extracted from observations along

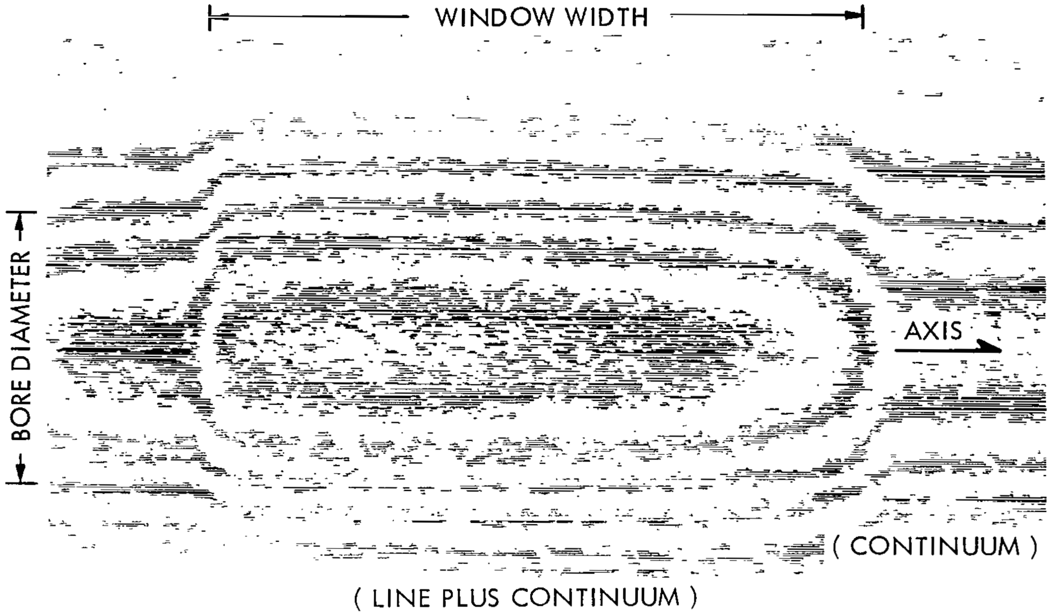

(a) Symmetric conditions.

(b) Asymmetric conditions.

Figure 5.- Isodensity traces of arc column in vicinity of 4300 ArI line radiation on underlying continuum tends to define extent of window which is serving as a slit for this data.

chord length by mathematical techniques often referred to as inversions since they either involve finding inverse integral transforms or the inverse matrix of a linear transformation.

In this section the Abel integral equation will be derived from basic energy and geometry considerations. The extent to which the requisite geometry can be approximated in practice because of optical limitations is then discussed.

Derivation of the Abel Equation

When the collecting optics are highly collimated, the inversion problem can be stated and solved as an Abel integral transform. Consider the energy collected by a rectangular aperture viewing along a chord length as in figure 6.

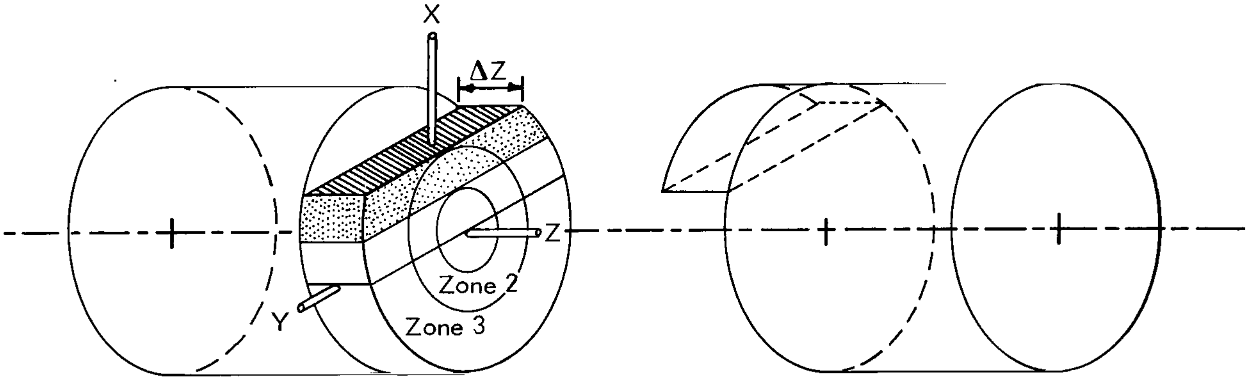

(a) Cylindrical lamina showing second rectangular swath observed under ideal Abel conditions.

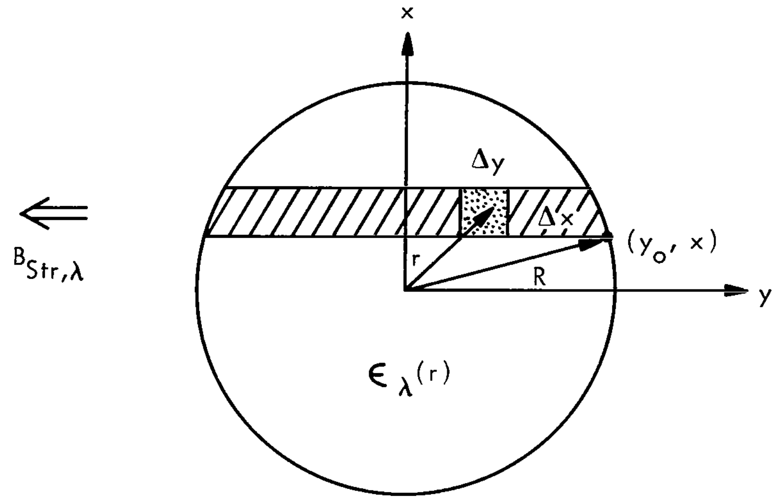

(b) Axial view of cylindrical emitter.

Figure 6.- Source geometry.

Assume, subject to later analysis, that no convergence is introduced by the optics and, furthermore, that all volume elements are equally effective in contributing to the signal (optically thin implication). The aperture cannot detect the depth of the source and the intensity may be interpreted as emanating from a strip having a certain brightness or steradiancy. This approach is reasonable since absolute intensity is determined by comparison with the steradiancy of a tungsten filament. Let $B_{Str,\lambda}$ be the specific intensity or spectral steradiancy of the source. If $\epsilon_\lambda(r)$ is the spectral emission coefficient, then for a slab of height Δz as shown in figure 6

$$B_{Str,\lambda}(x)\ \Delta x\ \Delta z = \sum_{-y_o}^{y_o} \epsilon_\lambda(r)\ \Delta x\ \Delta z\ \Delta y \tag{1}$$

Since $\Delta x\ \Delta z$ is uniform and divides evenly from both sides, and reflection symmetry is used after proceeding to the limit of the sum,

$$B_{Str,\lambda}(x) = 2 \int_{y=0}^{y=y_o} \epsilon_\lambda(r)\ dy$$

But $y = (r^2 - x^2)^{1/2}$ and, for fixed x, $dy = r(r^2 - x^2)^{-1/2}\ dr$. Consequently,

$$B_{Str,\lambda}(x) = 2 \int_{r=x}^{r=R} \frac{\epsilon_\lambda(r)\ r\ dr}{(r^2 - x^2)^{1/2}} \tag{2}$$

Since the left-hand side is measured, one has an integral equation for the unknown quantity. This is a particular example of a class of integral equations known as Abel equations. The kernel is singular because of the lower limit. The solution, although well known, will be outlined.

Let $\alpha = r^2$ and $\beta = x^2$. If r is written in terms of α and substituted in $\epsilon(r)$, a new functional form results which is designated by an overbar; hence,

$$\epsilon(r) \equiv \bar{\epsilon}(\alpha) = \bar{\epsilon}(r^2) \tag{3}$$

and similarly,

$$\bar{B}_{Str,\lambda}(\beta) \equiv B_{Str,\lambda}(x) \tag{4}$$

The integral equation is thus transformed to

$$\bar{B}_{Str,\lambda}(\beta) = \int_{\alpha=\beta}^{\alpha=R^2} \frac{\bar{\epsilon}(\alpha)\, d\alpha}{(\alpha - \beta)^{1/2}}$$

Multiply both sides of this equation by $d\beta(\beta - p)^{-1/2}$ and integrate from $\beta = p$ to $\beta = R^2$. Then

$$\int_{\beta=p}^{\beta=R^2} \frac{\bar{B}_{Str,\lambda}(\beta)}{(\beta - p)^{1/2}}\, d\beta = \int_{\beta=p}^{\beta=R^2} \frac{d\beta}{(\beta - p)^{1/2}} \int_{\alpha=\beta}^{\alpha=R^2} \frac{\bar{\epsilon}(\alpha)\, d\alpha}{(\alpha - \beta)^{1/2}}$$

$$= \int_{\beta=p}^{\beta=R^2} d\beta \int_{\alpha=\beta}^{\alpha=R^2} \frac{\bar{\epsilon}(\alpha)\, d\alpha}{(\beta - p)^{1/2}(\alpha - \beta)^{1/2}}$$

The integrand is some function of α and β, for example, $f(\alpha,\beta)$, and the order of integration suggested is that β is held fixed and α varied from the line $\alpha = \beta$ to $\alpha = R^2$ as shown in figure 7(a). The same "area" is covered by adding strips at constant α as in figure 7(b) with β going from p to α. Thus,

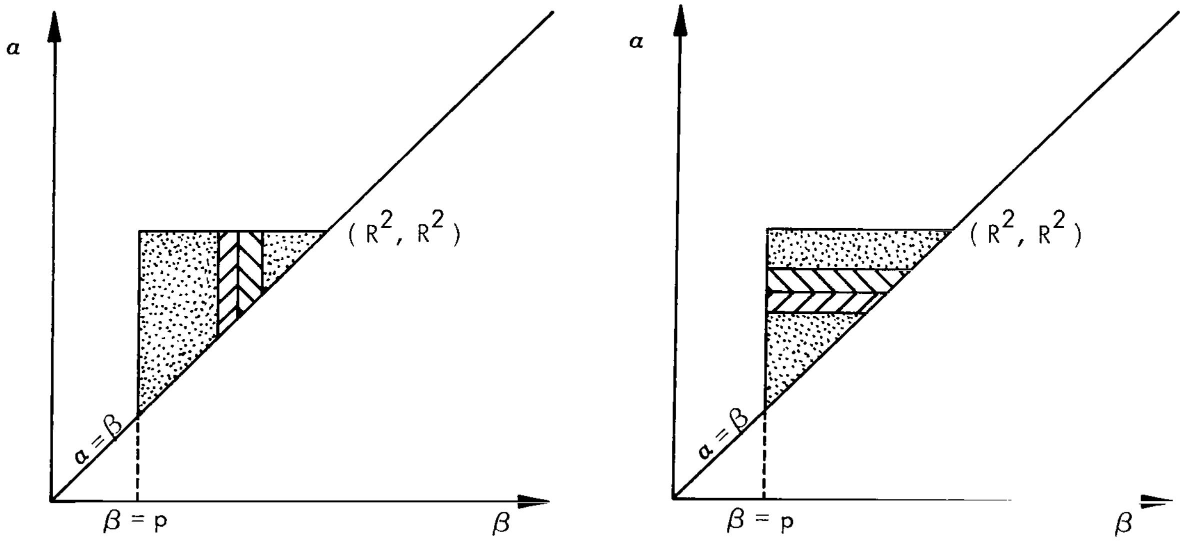

(a) Summing vertical strips.

(b) Summing horizontal strips.

Figure 7.- Strips used to define "area" of integration in the Abel derivation.

$$\int_{\beta=p}^{\beta=R^2} \frac{\bar{B}_{Str,\lambda}(\beta)}{(\beta - p)^{1/2}}\, d\beta = \int_{\alpha=p}^{\alpha=R^2} d\alpha \int_{\beta=p}^{\beta=\alpha} \frac{d\beta\,\bar{\epsilon}(\alpha)}{(\beta - p)^{1/2}(\alpha - \beta)^{1/2}}$$

$$= \int_{\alpha=p}^{\alpha=R^2} \bar{\epsilon}(\alpha)\, d\alpha \int_{\beta=p}^{\beta=\alpha} \frac{d\beta}{(\beta - p)^{1/2}(\alpha - \beta)^{1/2}}$$

The last integral is tabulated (ref. 9, no. 195.01) as

$$2 \tan^{-1}\sqrt{\frac{\beta - p}{\alpha - \beta}}\,\Bigg|_{\beta=p}^{\beta=\alpha} = 2 \tan^{-1}(+\infty) - 2 \tan^{-1}(0) = \pi$$

By use of this result, the equation reads

$$\int_{\beta=p}^{\beta=R^2} \frac{\bar{B}_{Str,\lambda}(\beta)}{(\beta - p)^{1/2}}\, d\beta = \pi \int_{\alpha=p}^{\alpha=R^2} \bar{\epsilon}(\alpha)\, d\alpha$$

Differentiate both sides with respect to p to obtain

$$\frac{d}{dp}\int_{\beta=p}^{\beta=R^2} \frac{B_{Str,\lambda}(\beta)}{(\beta - p)^{1/2}}\, d\beta = -\pi\bar{\epsilon}(p)$$

or

$$\bar{\epsilon}(p) = -\frac{1}{\pi}\frac{d}{dp}\left[\int_{\beta=p}^{\beta=R^2} \frac{\bar{B}_{Str,\lambda}(\beta)}{(\beta - p)^{1/2}}\, d\beta\right] \tag{5}$$

Let $p = r^2$ and recover the initial variables to obtain

$$\epsilon(r) = -\frac{1}{2\pi r}\frac{d}{dr}\left[2\int_{x=r}^{x=R} \frac{B_{Str,\lambda}(x)}{(x^2 - r^2)^{1/2}}\, x\, dx\right] \tag{5a}$$

This form is used by Barr (ref. 10) as a starting point for his numerical evaluation since smoothing can be done prior to numerical differentiation. The more common form is obtained by integrating equation (5) by parts before differentiating. Let

$$u = \bar{B}_{Str,\lambda}$$

$$dv = (\beta - p)^{-1/2}\, d\beta$$

Then

$$du = \frac{d\bar{B}_{Str,\lambda}}{d\beta}\, d\beta$$

$$v = 2(\beta - p)^{1/2}$$

and

$$\bar{\epsilon}(p) = -\frac{1}{\pi}\frac{d}{dp}\left[2\bar{B}_{Str,\lambda}(\beta)\,(\beta - p)^{1/2}\Big|_{\beta=p}^{\beta=R^2} - 2\int_{\beta=p}^{\beta=R^2} (\beta - p)^{1/2}\,\frac{d\bar{B}_{Str,\lambda}}{d\beta}\, d\beta\right]$$

$$= -\frac{1}{\pi}\frac{d}{dp}\left[2\bar{B}_{Str,\lambda}(R^2)\,(R^2 - p)^{1/2} - 2\int_{\beta=p}^{\beta=R^2} (\beta - p)^{1/2}\,\frac{d\bar{B}_{Str,\lambda}}{d\beta}\, d\beta\right]$$

But $\bar{B}_{Str,\lambda}(R^2) = B_{Str,\lambda}(R) = 0$ since R is defined as the point at which the signal is zero. Then

$$\bar{\epsilon}(p) = \frac{2}{\pi}\frac{d}{dp}\int_{\beta=p}^{\beta=R^2} (\beta - p)^{1/2}\,\frac{d\bar{B}_{Str,\lambda}}{d\beta}\, d\beta$$

$$= \frac{2}{\pi}\int_{\beta=p}^{\beta=R^2} -\frac{1}{2}(\beta - p)^{-1/2}\,\frac{d\bar{B}_{Str,\lambda}}{d\beta}\, d\beta$$

$$= -\frac{1}{\pi}\int_{\beta=p}^{\beta=R^2} \frac{1}{(\beta - p)^{1/2}}\,\frac{d\bar{B}_{Str,\lambda}}{d\beta}\, d\beta$$

Again letting $p = r^2$ and using original variables yields

$$\bar{\epsilon}(r^2) \equiv \epsilon(r) = -\frac{1}{\pi}\int_{x=r}^{x=R} \frac{1}{(x^2 - r^2)^{1/2}}\,\frac{dB_{Str,\lambda}}{dx}\, dx \qquad (6)$$

Although many papers have appeared on the numerical evaluation of this integral, only two will be cited. Bockasten (ref. 11) evaluates equation (6) directly in a rigorous fashion. Since experimental data are numerically differentiated in this method, fine zoning and low-noise data are required. Barr's method (ref. 10) of working with equation (5a) and smoothing the data prior to differentiation is used in this work. Barr compares the two approaches in his article.

Optical Considerations for Abel Inversion

To utilize these analytical results, the optics are arranged to project the small rectangular field stop of the system into the emitting source so that energy will be accepted from small swaths (see fig. 6(a)) along successive chord lengths of the source. Apertures in the system should be small enough to provide as many nonoverlapping swaths as possible since one is essentially representing a continuous function by a series of discrete points. The stops and optics quality must insure sharp focus for all points along the diameter of the source; otherwise, the volume elements would be unequally weighted contrary to the underlying assumption. In practice, stopping the system down to achieve the requisite depth of field and data point density is impeded by the onset of diffraction and/or poor signal-noise ratio.

Most published information relating to radial profile measurements deals with photoelectric output and the scanning slit aperture is located at the stigmatic plane of the spectrograph (entrance slit). When the photographic mode is used, the densitometer scanning spot as imaged into the source ultimately becomes the field stop. Consideration of figure 8 should clarify this point. The densitometer scanning beam with dimensions W_d by H_d intercepts an area of the processed plate. The transmission of the processed plate is uniquely related, through sensitometry, to the illuminance of the plate during its exposure. By neglecting the spread function of the emulsion in comparison with scanning

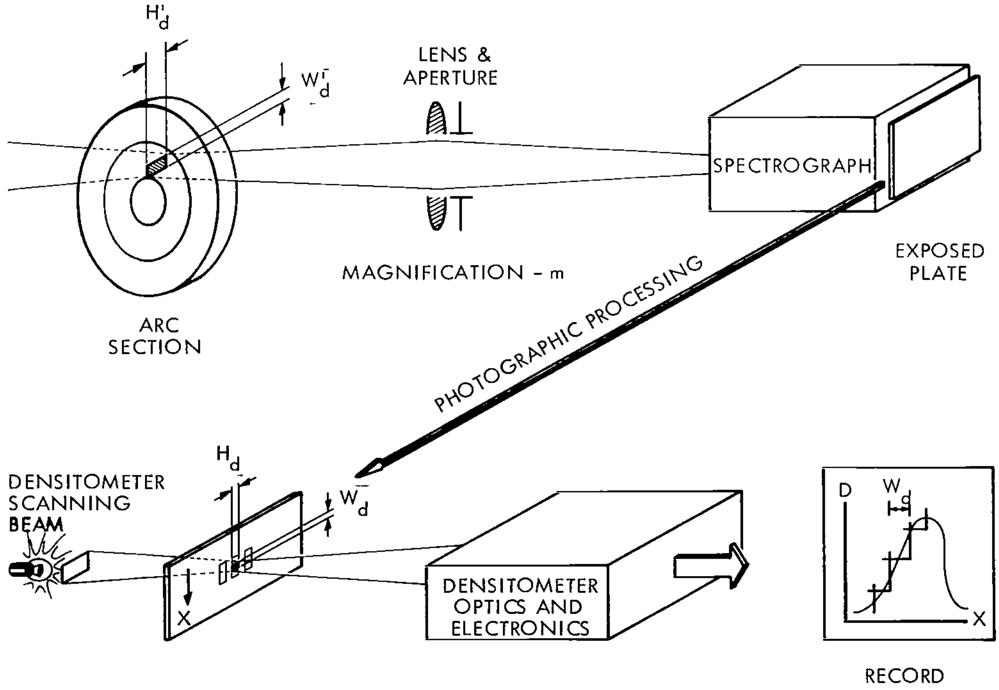

Figure 8.- Illustration of Abel inversion concept with film mode.

slit dimensions, the latter can be thought of as imaged by the spectrograph and inversion optics into the volume emitter where it has a cross section W'_d by H'_d.

To assess the stigmatic quality of the spectrograph, a reticle that is graduated finer than the desired zone spacing is placed at the entrance slit. Its image is viewed in the film plane and examined for distortion. This examination is made either in white light by using zeroth order or in monochromatic light (for example, Hg green line) by using the dispersion mode.

The optical layout is sketched in figure 9(a) and pictured in figure 9(b). The "T" arrangement allows for absolute intensity calibration with good repeatability and minimal effort. The arc is mounted on a rotatable base so that it can be viewed axially or side-on. The optical train consists of a single lens L and aperture of diameter D. This aperture controls the energy throughput (aperture stop), degree of parallelism, and depth of field. The depth of field dependence on D will now be considered, the analysis of the convergence aspects being deferred to the next section.

Let ϵ be the minimum resolvable dimension on the film or perhaps, to be safe, some multiple of it, and S' the lens-to-slit plane distance. Then with m, the linear magnification of the lens system, the following relationship for the depth of field Δ is derived in appendix A:

$$\Delta = \frac{1}{m^2} \frac{2S'\epsilon}{D}$$

In practice, the source is often very small and no significant demagnification can be tolerated. The quantity S' is reasonably determined by spatial requirements of the laboratory and ϵ does not vary significantly for available spectroscopic plates. By elimination then, the depth of field is mainly regulated by the lens of diameter D. If 2R is the diameter of the arc column, then

$$\frac{1}{m^2} \frac{2S'\epsilon}{D} \geqq 2R$$

or

$$D \leqq \frac{S'\epsilon}{m^2 R}$$

The diameter D must not be reduced to the point where diffraction deteriorates the image of the arc column on the slit. For arcs, it is feasible to look for diffraction effects by placing a white card at the entrance plane. For nonvisible light or weak sources, one might insure that $\lambda S' < D^2$ (ref. 12).

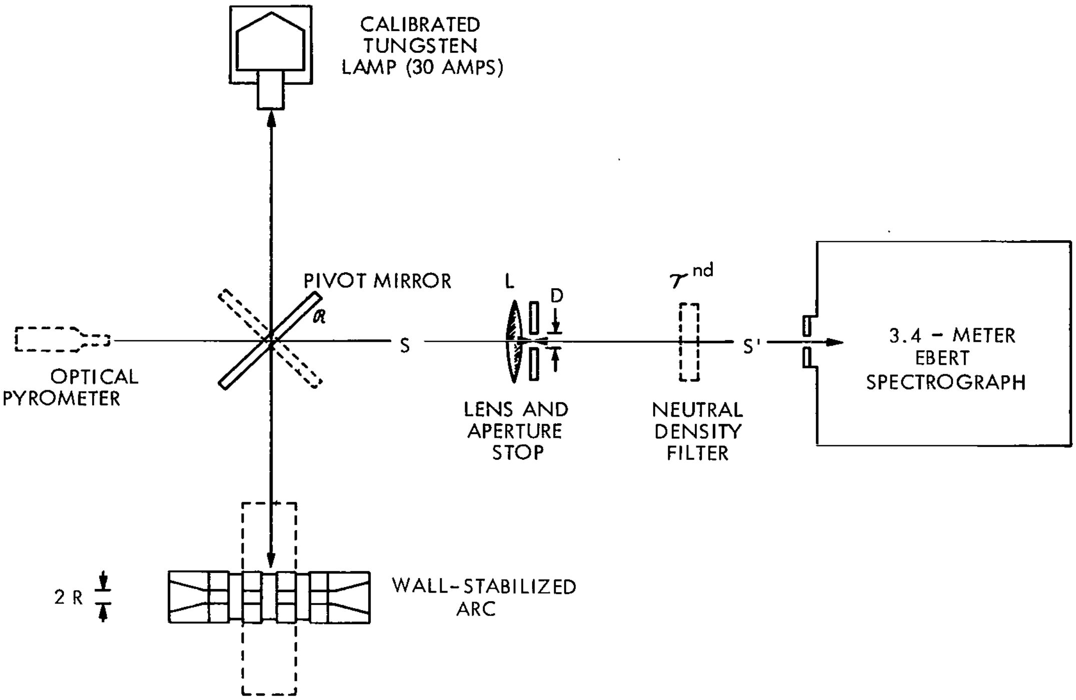

(a) Optical layout.

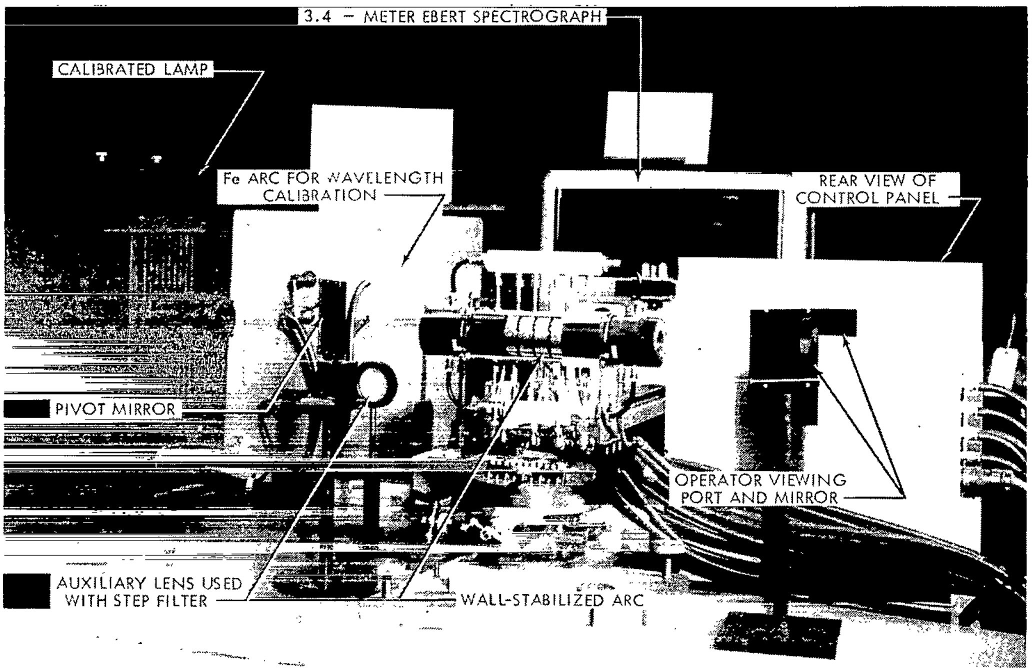

L-71-5864

(b) Partial view of the experimental layout with the arc in the end-on position.

Figure 9.- Experimental setup.

Estimate of Nonparallelism

In figure 10, a typical volume of intersection is sketched with convergence present. It should be contrasted with figure 6(a). An expression for the effective slit width W_{eff} will now be derived. The effective width on the side of the source nearest the spectrograph is called the front effective width and would be subscripted with an f to contrast it with the back effective width $W_{eff,b}$ and usually the subscript eff will be suppressed to condense notation. The width W_b is always larger and will determine the distance between observation points and hence the number of zones possible with a given geometry. The result will be useful in estimating the relative volume error made when the Abel requirements are compromised.

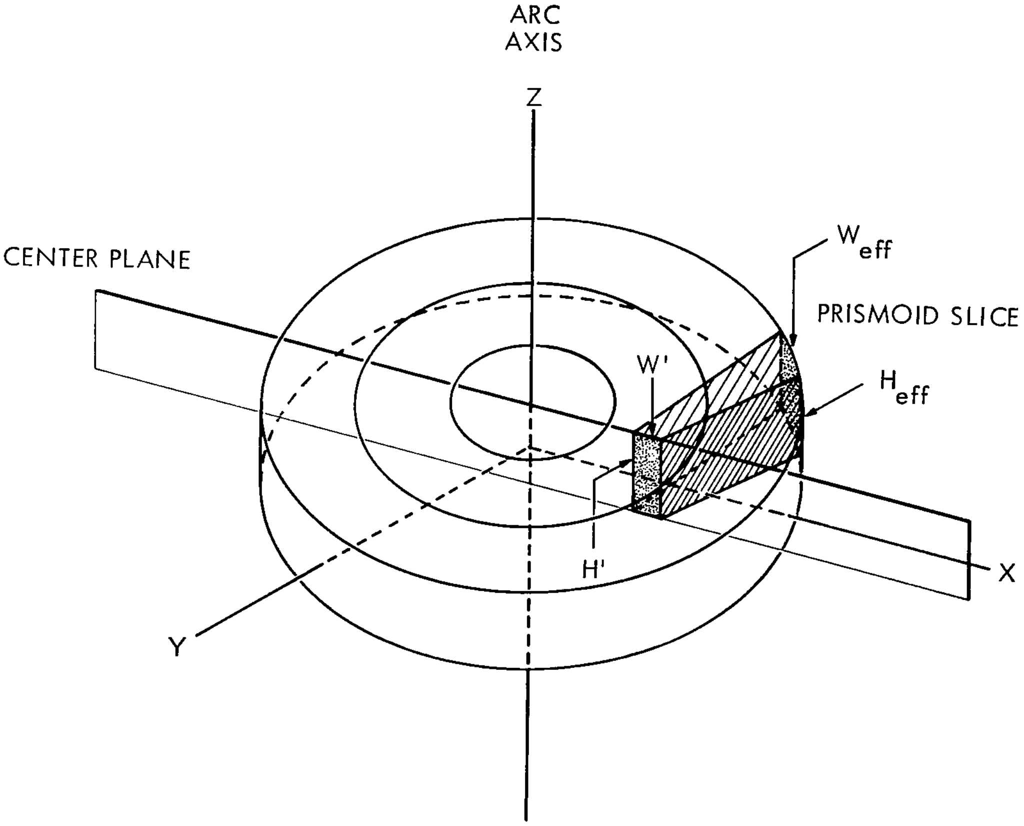

Figure 10.- Sketch of prismoid of intersection for actual case having finite f numbers.

In figure 11(a) the extreme rays are sketched for one dimension of the scanning slit when it is centrally positioned. The relative dimensions are distorted to emphasize convergence. Clearly, a conservative estimate for W_b is the chord whose half length is ab. In figure 11(b) construction lines and symbols used to relate ab to known quantities are provided.

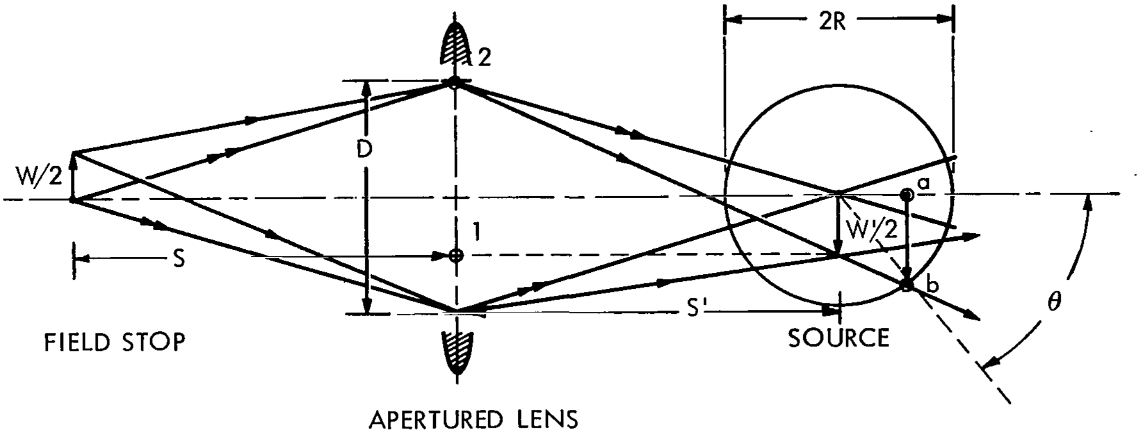

(a) Extreme rays for swath 1.

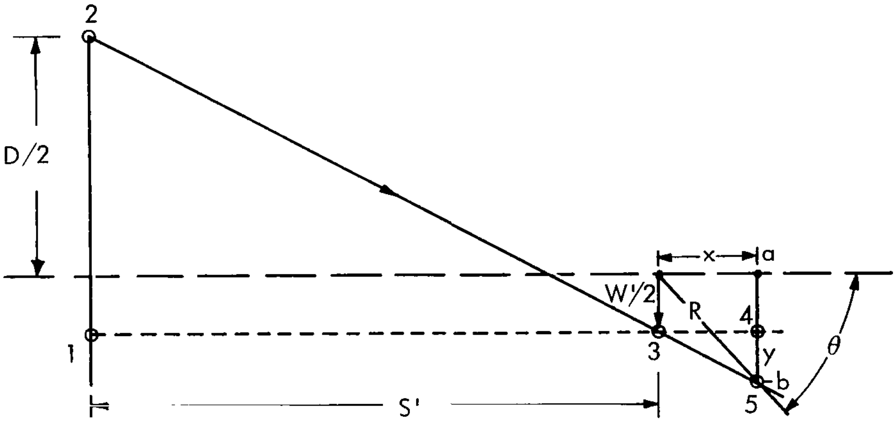

(b) Lines used in derivation of $W_{eff,b}$.

Figure 11.- Derivation of $W_{eff,b}$.

As a result,

$$W_{eff,b} = W' + 2y$$

Considering triangles 123 and 345 (fig. 11(b)),

$$\frac{y}{x} = \frac{\frac{D}{2} + \frac{W'}{2}}{S'}$$

or

$$y = \frac{\frac{D}{2} + \frac{W'}{2}}{S'} x$$

By noting that $x = R \cos \theta = R(1 - \sin^2 \theta)^{1/2}$,

$$W_b = W' + \frac{D + W'}{S'} R(1 - \sin^2 \theta)^{1/2}$$

But if $n = \frac{R}{W_b}$ is the number of zones, then $\sin^2 \theta \approx \left(\frac{W_b}{2R}\right)^2 = \frac{1}{4n^2}$ and

$$W_b = W' + \frac{R(D + W')}{S'} \left(1 - \frac{1}{4n^2}\right)^{1/2}$$

Even for a relatively coarse five zone case, the radical term is approximately 1 and need not be carried

$$W_b \approx W' + \frac{R(D + W')}{S'}$$

The quantity W_f is calculated in a similar fashion and introduces a minus sign in the parentheses and S' must become infinite to recover the Abel geometry. In practice S' is made large and D small, subject to the constraints listed in the preceding section. It is desirable to have an indication as to the effects that the finite optics will have on interpretations of emission coefficients. By using W_b as zone width and interpreting the data with Abel equations, the source volume collected is overestimated. Consequently, the energy per unit volume which is calculated will be lower than the true value. Furthermore, the error should be largest in the central hot zones where the volume is smallest. A precise calculation of the volume omissions involve triple integrals with limits set by the intersections of prismoids and cylinders as suggested in figure 10.

Since writing down the expression for the volume integrals is not particularly instructive, the following more tractable estimate is suggested. A volume element bounded from below by dA and from above by $f(x,y)$ is $f(x,y)\, dA$, and for finite volume $V = \iint f(x,y)\, dA$. If f is a slowly varying function of x and y as it would be on one of the faces of the prismoids, then f could be taken from the integral as approximately constant. In this spirit, consider figure 12(a) where a swath is depicted in projection and an enlarged view of the zone 1 in figure 12(b). The term W' is assumed to be centered

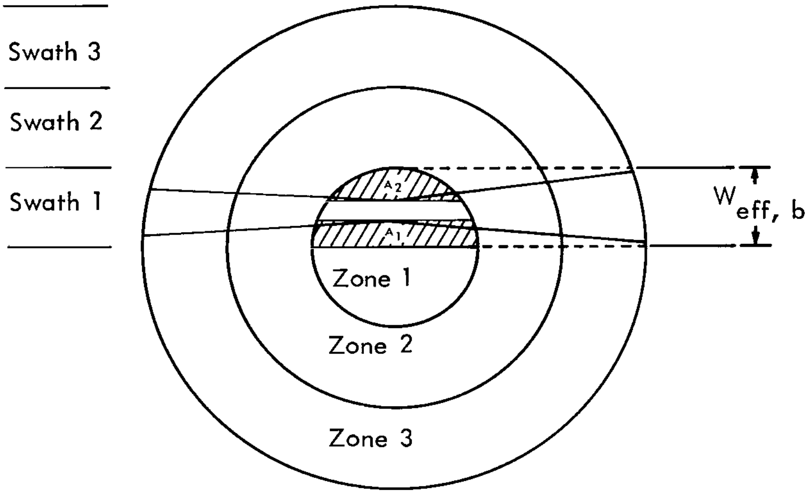

(a) Figure used to estimate relative error in volume measurement due to finite optics.

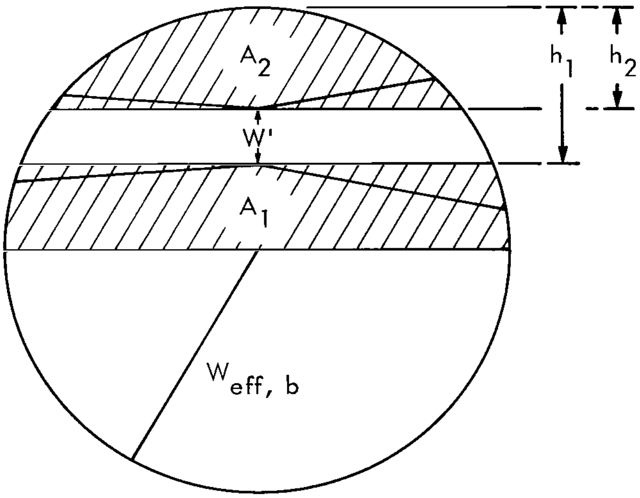

(b) Enlarged view of zone 1.

Figure 12.- Estimation of relative error.

in swath 1 for simplicity. It is apparent that the area omitted will be less than or equal to the hatched area $A_1 + A_2$. Then, reasoning as above, the relative volume error is taken as

$$\frac{\Delta V}{V} \approx \frac{2\Delta A}{\pi W_b^2} \leqq \frac{2(A_1 + A_2)}{\pi W_b^2}$$

From plane geometry (ref. 13, p. 12), recall that the area of a segment bounded by a chord a distance $R - h$ from the center of a circle having radius R is $R^2 \cos^{-1}\left(\frac{R - h}{R}\right) - (R - h)(2Rh - h^2)^{1/2}$. Since $h_1 = (W_b + W')/2$, then

$$A_1 = W_b^2\left[\frac{\pi}{2} - \cos^{-1}\left(\frac{W_b - W'}{2W_b}\right)\right] + \frac{W_b - W'}{2}\sqrt{\frac{3}{4}W_b^2 + \frac{W_bW'}{2} - \frac{W'^2}{4}}$$

Similarly, $h_2 = (W_b - W')/2$ giving

$$A_2 = W_b^2 \cos^{-1}\left(\frac{W_b + W'}{2W_b}\right) - \frac{W_b + W'}{2}\sqrt{\frac{3}{4}W_b^2 - \frac{W_bW'}{2} - \frac{W'^2}{4}}$$

Introduce these expressions in the relation $\Delta V/V$ and define $w \equiv \frac{W'}{W_b}$ which is the reciprocal of the effective slit dimension in units of its geometric image as determined from optics and obtain

$$\begin{aligned}\frac{\Delta V}{V} \leqq 1 &+ \frac{2}{\pi}\left[\cos^{-1}\left(\frac{1 + w}{2}\right) - \cos^{-1}\left(\frac{1 - w}{2}\right)\right] \\ &+ \frac{1}{2\pi}\left[(1 - w)\sqrt{(3 - w)(1 + w)} - (1 + w)\sqrt{(3 + w)(1 - w)}\right]\end{aligned}$$

By using the approximate expression for W_b, one obtains

$$w \approx \left(1 + \frac{D}{W'}\frac{R}{S'} + \frac{R}{S'}\right)^{-1}$$

The dimensionless ratios R/S' and D/W' quite clearly control the relative error. Note that if S' becomes infinite, w becomes 1 and the relative volume error is zero as it should be for the Abel case. If a rectangular scanning aperture is used, the expression should be tested for both slit dimensions. To guard against convergence problems, R/S' and D/W' should be chosen to make $\Delta V/V$ less than 5 or 10 percent. Figure 13 shows the dependence of $\Delta V/V$ on both D/W' and R/S'. For the data reported in this note D/W' was 1.6 mm/1.6 mm or 1, and R/S' was 3 mm/1000 mm or 0.003. It should be emphasized that this expression is approximate and that the curves should not be used to correct measured values.

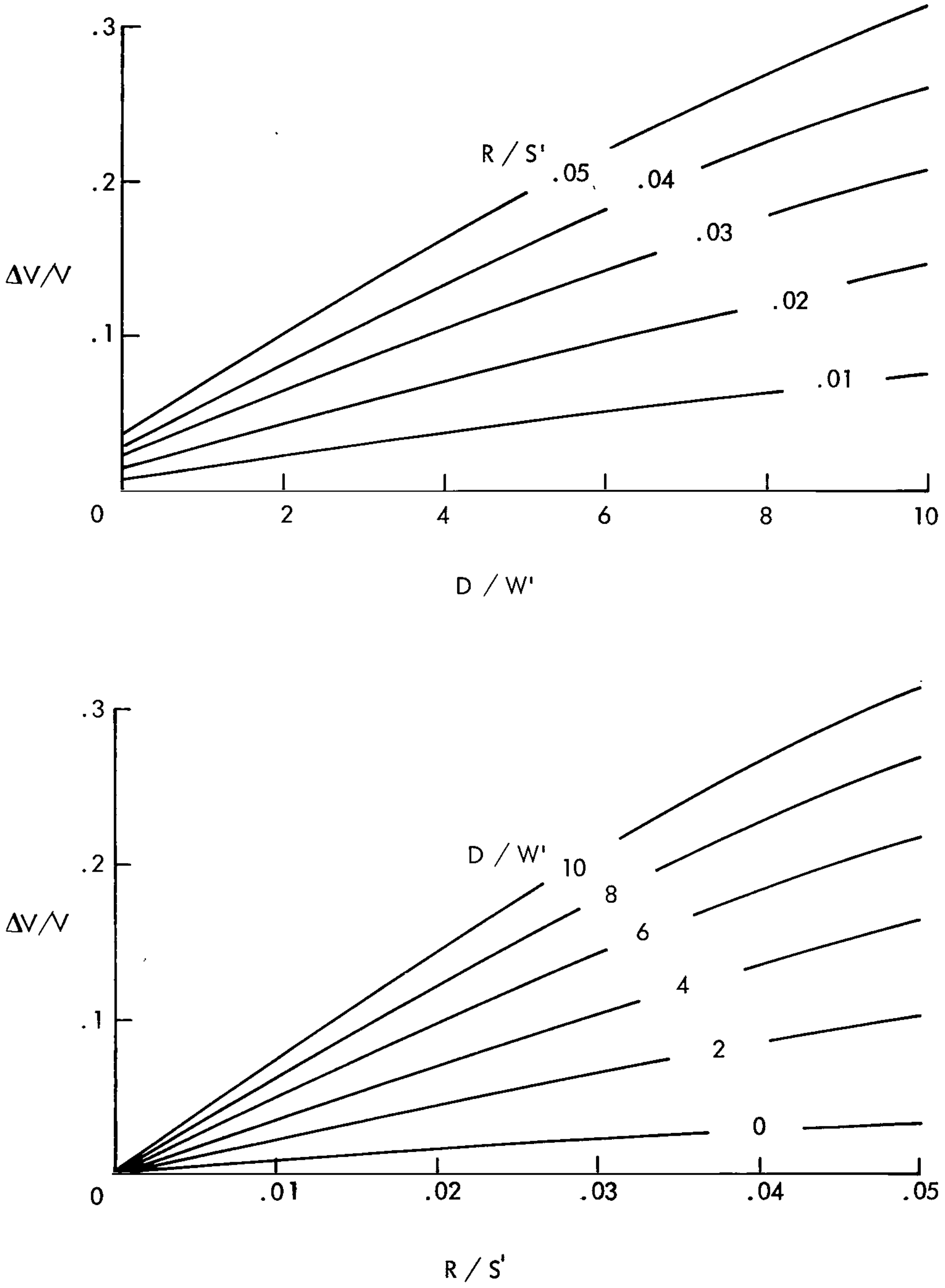

Figure 13.- Relative volume errors as a function of experimental parameters.

OPTICAL DEPTH CONSIDERATIONS

The solution of the radiative transfer equation for slab geometry in a collision-dominated gas having a Planckian source function (based on ref. 7, eq. (69.9)) is given by

$$I_\lambda = B^o_{Str,\lambda}(T)\left[1 - \exp\left(-k_\lambda x\right)\right]$$

where $B^o_{Str,\lambda}(T)$ is the specific intensity of a black body at temperature T, x the geometric depth into the slab, and k_λ is the spectral linear absorption coefficient. It is tacitly assumed when inverting the data that each photon emitted in the source escapes from it without reabsorption. Mathematically, this relationship holds if the optical depth $k_\lambda x$ is small compared with 1 so that two terms in the Maclaurin expansion of the exponential suffice to represent it, namely,

$$I^{thin}_\lambda \approx B^o_{Str,\lambda}(T) \left[1 - \left(1 - k_\lambda x\right)\right]$$

for then the signal increases in direct proportion to the depth of source viewed.

Theory

The line is fully characterized by its absorption coefficient, which it is convenient to write as

$$k_\lambda = \mathcal{L}(\lambda - \lambda_o)S$$

Thus, spectral detail as carried by the normalized line shape $\mathcal{L}$, that is,

$$\int_{-\infty}^{\infty} \mathcal{L}(\lambda - \lambda_o)\, d(\lambda - \lambda_o) = 1$$

is explicitly separated from the strength of absorption determined by the integrated absorption S. An explicit expression for S when written in terms of wavelength is

$$S = \lambda_o{}^2 \pi r_e N_l f_{l \rightarrow u}$$

The specific intensity of each line "grows" with optical depth in its own peculiar way which must be determined empirically and results in its curve of growth (ref. 14, p. 64). The region of this curve which is linear in x identifies the optically thin domain. In practice, it is often sufficient to calculate k_λ by using an approximate model to insure that the truncated series expansion is valid. A popular expression is the Voigt form (ref. 15, eq. (3-34)) which is the convolution of dispersion and Gaussian shapes parameterized by

$$a = \frac{w_{col}}{w_{Dop}}\left(\log_e 2\right)^{1/2}$$

where w_{col} and w_{Dop} are, respectively, the full widths at half maximum for the collision and Doppler broadened components. The Gaussian profile is recovered from the Voigt formula when a is zero, and the dispersion profile when a is infinite. Although the Voigt formula incorporates the overall general aspects of line broadening, its approximate nature should be stressed. Its symmetric form suggests that only those collisions which terminate the emitting wave train are included in the collision broadening, whereas observed Stark profiles display a strong asymmetry and shift attesting to the vast number of the collisions which only alter the phase of the wave train. To show its usefulness, a rough estimate of the peak absorption expected for a line in the plasma will be given.

To be specific, consider the 4300 ArI line as radiated from a 10 000 K argon plasma at a total pressure of 1 atmosphere. Penner (based on ref. 15, eq. (4-37)) shows that

$$k_{\lambda_o} = \frac{2S}{w_{Dop}}\sqrt{\frac{\log_e 2}{\pi}}\exp(a^2)\left[1 - \mathrm{erf}(a)\right]$$

The composition data of Popenoe and Shumaker (ref. 16) were used to obtain table I. If λ_o is the line center in angstroms, T, the absolute temperature, and A, the mass in atomic mass units, then the Doppler half intensity width is given as (ref. 17, p. 67)

$$w_{Dop} = 7.11 \times 10^{-7}\sqrt{\frac{T}{A}}\,\lambda_o,\ \text{angstroms}$$

$$= 7.11 \times 10^{-7}\sqrt{\frac{10\,000}{40}}\,4300 = 0.048\ \text{angstrom}$$

The collision broadening is mainly electronic Stark broadening which is obtained from Griem (ref. 1, p. 492), and by referring to table I for the electron density

$$w_{col} = \frac{2w(10\,000\ \text{K})N_e}{1 \times 10^{16}},\ \text{angstroms}$$

$$= \frac{2(0.106)\left(1.511 \times 10^{16}\right)}{1 \times 10^{16}} = 0.320\ \text{angstrom}$$

The a parameter is now easily evaluated as 5.6. Since the absorption oscillator strength is related to the transition probability through (ref. 18)

$$f_{l\to u} = 1.4992 \times 10^{-16}\lambda^2 \frac{g_u}{g_l} A_{u\to l}$$

with λ in angstroms, then using $0.411 \times 10^6 \pm 11$ percent $\sec^{-1}$ for $A_{u\to l}$ (ref. 11)

$$f_{l\to u}^{4300\ \mathrm{ArI}} = 1.4992 \times 10^{-16}(4300)^2 \frac{5}{3}(0.411 \times 10^6) = 0.0019$$

The integrated absorption then becomes

$$S = (4.3 \times 10^{-5})^2(3.14159)(2.8179 \times 10^{-13})(2.930 \times 10^{12})(0.0019)$$

$$= 9.1 \times 10^{-12} \text{ (dimensionless)}$$

giving the peak linear absorption coefficient estimate of

$$k_{\lambda_o}^{4300\ \mathrm{ArI}} = \frac{2(9.1 \times 10^{-12})}{0.048 \times 10^{-8}}\sqrt{\frac{\log_e 2}{\pi}} \exp\left[(5.6)^2\right]\left[1 - \mathrm{erf}(5.6)\right]$$

$$= 0.0018 \text{ cm}^{-1}$$

Since x_{max} is on the order of the diameter of the column for the inversion work, $2Rk_{\lambda_o} \approx 0.001 << 1$ and the optical thin assumption seems to be well justified.

Experiment

The arc configuration allows for empirical verification of the optical depth estimate and, more significantly, for a direct evaluation when line-shape information is unavailable. The arc chamber is rotated so that it can be viewed axially. By looking at a small cross section, isothermal zones of plasma are viewed. A concave mirror is placed behind the column at a distance 2F from the arc midplane where F is the focal length of the mirror and in such a way that, when uncovered, it directs the arc radiation incident upon it back through the system and onto the entrance slit. The mirror is alined by directing a He-Ne laser beam through the film plane of the spectrograph. It is reflected from the internal optics and out the entrance slit, down the optical axis of the system, and through the arc chamber to the concave mirror. The mirror is adjusted to cast the beam back through the entrance slit. Since the optical lever arms are on the order of several meters, it is felt that this arrangement insures very good alinement. From consideration of the sketch of figure 14 with the end windows having transmission τ, the mirror having reflectivity $\mathcal{R}$, and $\tau^{pl} = e^{-kx}$ representing the plasma transmission, it is evident that the ratio of double-path to single-path signals should be $1 + \tau^2 \mathcal{R} \tau^{pl}$, all quantities being spectral. Figure 14 reproduces an actual data trace. At selected points, the single-path signal is multiplied by $1 + \mathcal{R}\tau^2$ and is plotted with error bars estimated from repeatability tests. Since the reflectivity and transmission values are known, the ratios of double-path to single-path signals from figure 14 allows the determination of τ^{pl} which can be solved for k_λ. Spectral resolution was adequate enough to allow measurement of peak line values, and k_{λ_0} for 4300 ArI was measured as 0.14 per cm and confirms the optical thin analysis. The discrepancies in k_{λ_0} however, underscore the caution of relying over much on estimates using approximate line shapes.

The usefulness of the experimental arrangement will be most evident when constituents are tested which have a large spread in lower energy levels and whose spectrum should therefore display a wider variation of spectral absorptivity than is afforded by argon.

TEMPERATURE MEASUREMENTS

Absolute Line Intensity Method

The temperature measurement rests ultimately on a comparison of the brightness or steradiancy of an atomic line with that of a tungsten filament, the latter calculable from observing its brightness temperature. Whereas the total power output of the line I^L is understandable from energy principles alone, a calculation of its spectral steradiancy requires a knowledge of its line shape. It is not immediately obvious how this strongly wavelength-dependent term is to be measured.

Consider the problem of measuring the spectral specific intensity I_λ^L. It is useful to distinguish further the true quantity as would be detected with infinite resolution from the measured quantity under finite resolution. This distinction is made with appended superscripts. A spectrograph distributes a monochromatic beam of light of wavelength λ_0 over a range of wavelengths whose functional dependence is designated by $g(\lambda - \lambda_0)$ and is called the apparatus function. The true and measured distributions are related through a convolution; namely,

$$I_\lambda^{L,meas} = \int_{-\infty}^{\infty} I_{\lambda'}^{L,true} g(\lambda - \lambda')\, d\lambda'$$

The apparatus function is determined by scanning a very narrow atomic line as would be emitted, for example, from a low-pressure microwave discharge. Then

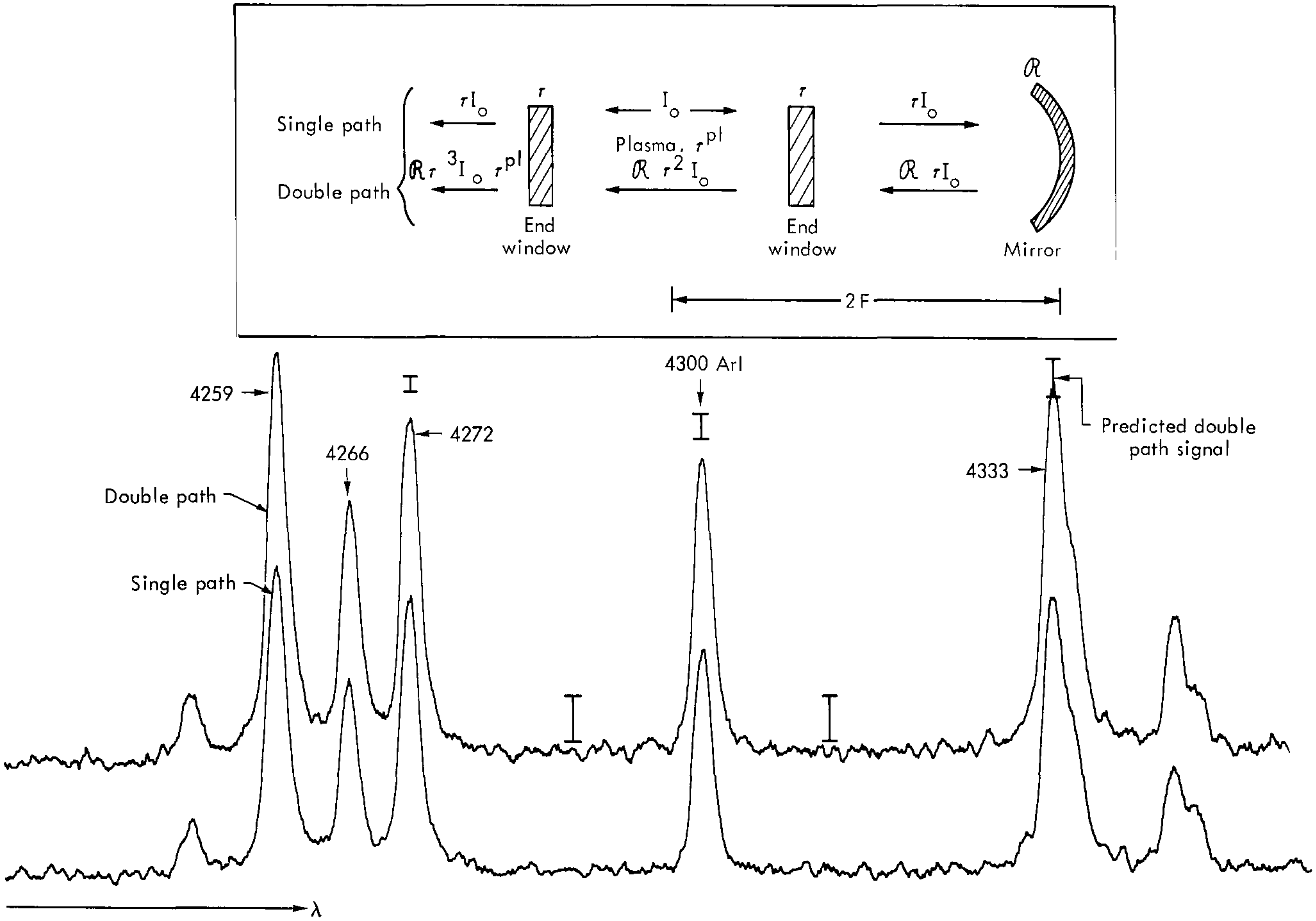

Figure 14.- Sketch of scheme for empirically determining optical depth and sample of data.

$$I_{\lambda'}^{L,\text{true}} = (\text{Constant})\left[\delta(\lambda' - \lambda_o)\right]$$

and

$$I_{\lambda}^{L,\text{meas}} = (\text{Constant})\left[g(\lambda - \lambda_o)\right]$$

The function g is usually normalized so that its effect will be to redistribute while conserving energy. If the entrance slit of a spectrograph is very wide, a rectangular apparatus function $g_{\square}$ obtains

$$g_{\square}(\lambda - \lambda_o) = \frac{1}{W} \qquad \left(|\lambda - \lambda_o| \leqq \frac{W}{2}\right)$$

$$g_{\square}(\lambda - \lambda_o) = 0 \qquad \left(|\lambda - \lambda_o| > \frac{W}{2}\right)$$

where W is the spectral slit width obtained by multiplying the slit dimension by the reciprocal linear dispersion of the instrument. To this approximation

$$\begin{aligned} I_{\lambda}^{L,\text{meas}} &= \int_{-\infty}^{\infty} g_{\square}(\lambda - \lambda')I_{\lambda'}^{L,\text{true}}\, d\lambda' \\ &= \frac{1}{W}\int_{-W/2}^{W/2} I_{\lambda'}^{L,\text{true}}\, d\lambda' \end{aligned}$$

and if the extent of the line is much less than W, little accuracy is lost by extending the limits to infinity to yield

$$I_{\lambda}^{L,\text{meas}} \approx \frac{1}{W}\int_{-\infty}^{\infty} I_{\lambda'}^{L,\text{true}}\, d\lambda' = \frac{I^{L,\text{true}}}{W}$$

To summarize, whenever the spectral slit width can be made much wider than the true line width to justify the redefined limits, the total line output follows by multiplying the spectral quantity at any point within the signal by W. Unfortunately, for the strongly broadened lines in plasmas, this must be done with some reservation. In figure 15 a trace of a mercury line suitable for apparatus function determination is shown along with an argon line as it appears in an arc plasma. Both traces are taken with the same spectrograph settings and differ only in that the arc line is not narrow with respect to the spectral slit width – it is, in fact, comparable with it.

To solve this problem, a rectangular apparatus function is generated by using wide slits, and the total intensity derived on this basis is empirically corrected. This

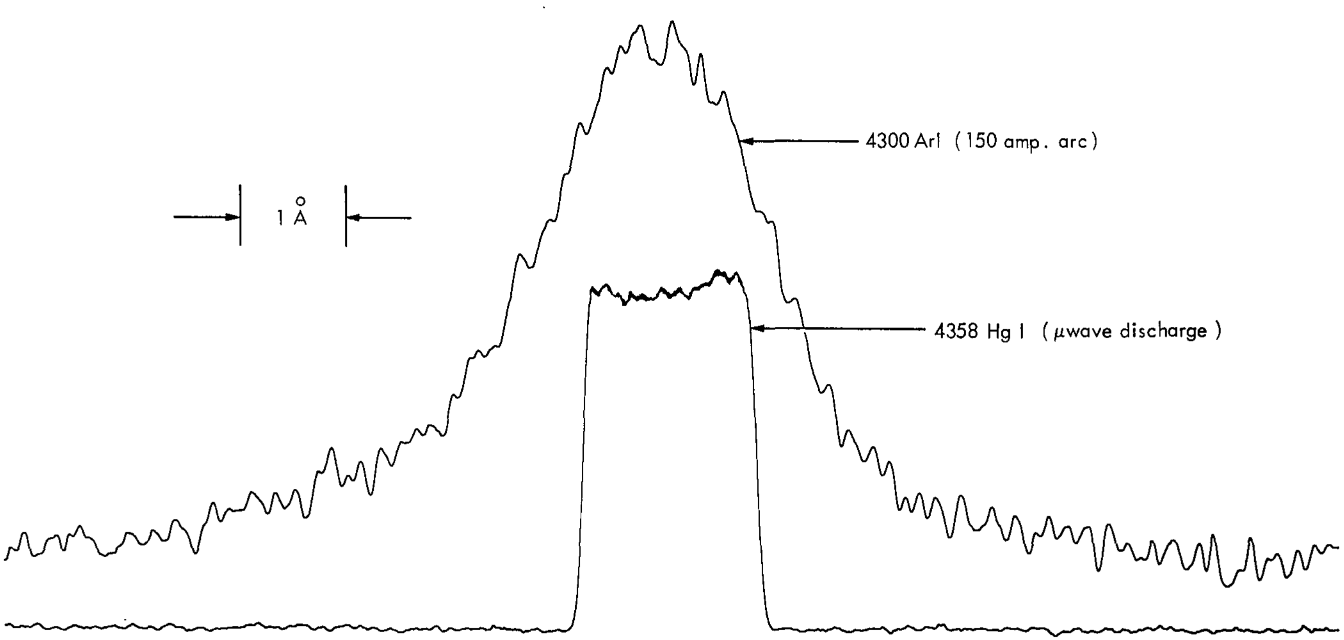

Figure 15.- Effect of line width on observed traces using an instrument with rectangular apparatus function.

procedure will now be described. Separating the defining integral for total intensity I^L into parts gives

$$I^L = \int_{-\infty}^{\infty} I_\lambda^{L,meas}\,d\lambda = \int_{-\infty}^{-W/2} I_\lambda^{L,meas}\,d\lambda + \int_{-W/2}^{W/2} I_\lambda^{L,meas}\,d\lambda + \int_{W/2}^{\infty} I_\lambda^{L,meas}\,d\lambda$$

The first and third integrals on the right-hand side are designated by ΔA. It is convenient to center the integrals at λ_o. In figure 16 the different contributions are identified by hatching. Thus,

$$I^L = \int_{-W/2}^{W/2} I_\lambda^{L,meas}\,d\lambda + \Delta A$$

and by making the rectangular apparatus function assumption,

$$I^L = W \cdot I_{\lambda_o}^{L,meas} - \Delta A_\square + \Delta A$$

$$= W \cdot I_{\lambda_o}^{L,meas} + \Delta I = \left(1 + \frac{\Delta I}{I_\square^L}\right) I_\square^L \equiv C I_\square^L$$

where $W \cdot I_{\lambda_o}^{L,meas}$ has been abbreviated to $I_\square^L$, and the last equality defines the correction factor C. Figure 16 also identifies ΔI in terms of areas under observed traces. To reiterate, W, the spectral slit width, is obtained by tracing a narrow line from a low-pressure discharge. The arc line is read up by using a rectangular apparatus function and corrected by using the empirical C determined by planimetry. The empirical C must be redetermined for each line and whenever conditions are expected to change the line shape. At high currents, the correction can amount to several hundred degrees.

The procedural aspects of "inverting" photographically have been commented upon with regard to figure 8. It is now appropriate to enlarge that discussion to indicate how the absolute intensity information is obtained. The cylindrical arc column is imaged on and perpendicular to the entrance slit having dimensions W_s by H_s. The instrument introduces no demagnification and is sufficiently stigmatic; therefore, the image on the plate in the vicinity of a spectral line will roughly have dimensions W_s by H_s. The edge will be diffused along the dispersion dimension because of the nonmonochromatic nature of the line which was corrected for above and along the height dimension because the radiance of the arc decreases as chords closer to the outer edge are viewed. To simplify the analysis, figure 17 portrays the density of developed grains by a contour map. Also shown are the dimensions and scan direction of the densitometer slit W_d by H_d. The dimension H_d is taken small compared with W_s so that the trace will be related to

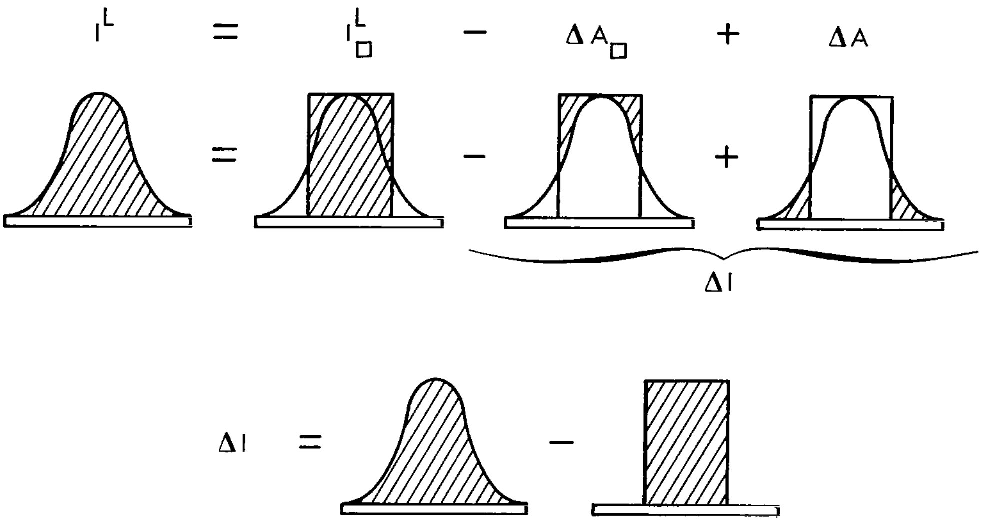

(a) Identification of integrals.

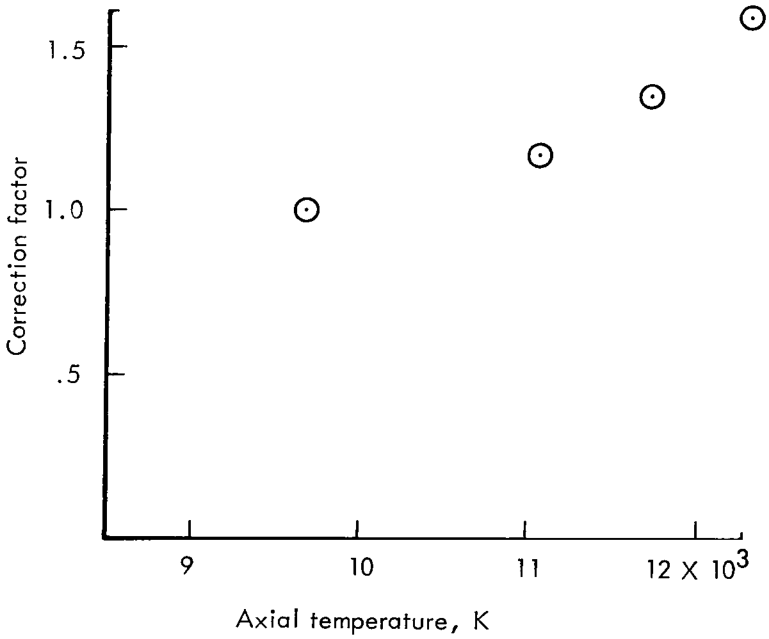

(b) Variation of line correction factor C with axial temperature.

Figure 16.- Line correction factor.

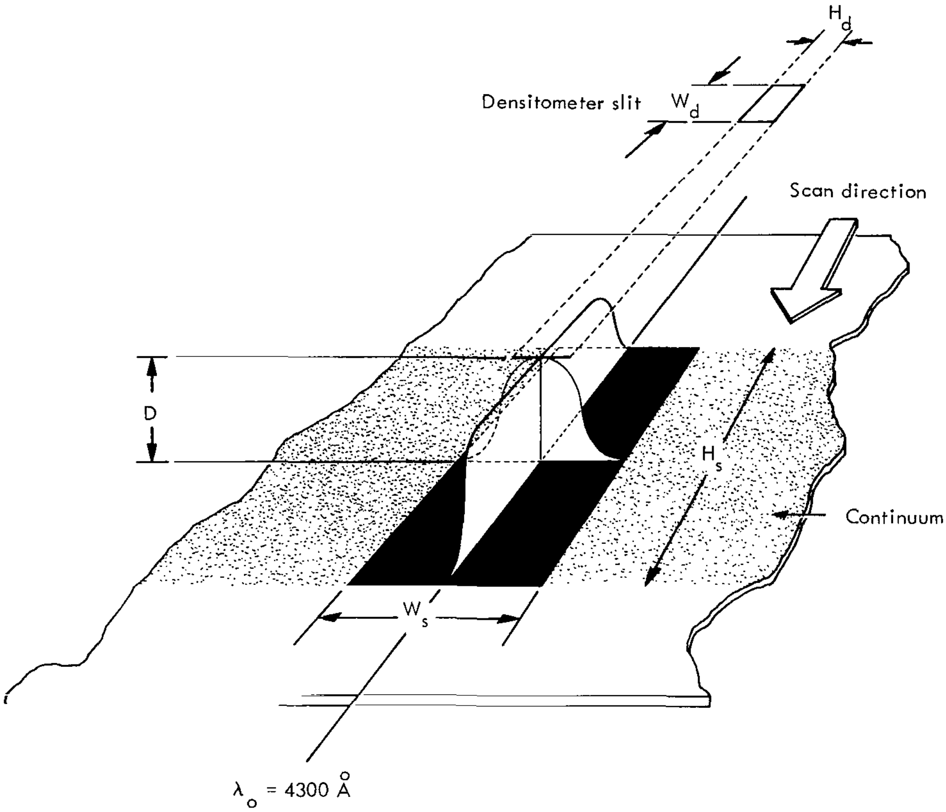

Figure 17.- Contours of developed line showing photographic inversion technique.

the spectral intensity at λ_0. The dimension W_d may be adjusted within the limits set by the desired inversion resolution and adequate signal-noise ratio. A spectral sensitometry strip is recorded on each plate to relate the densitometer signals to relative intensity. Care is taken to maintain chemical purity and temperature control during processing and a nitrogen burst system is used to agitate the developer as a safeguard against the Eberhard effect. The arc is much more intense than the tungsten filament to which it is compared and its exposure time orders of magnitude shorter. To guard against reciprocity failure, a neutral density filter having transmission τ^{nd} is introduced into the optic train for the arc exposure, its magnitude being chosen to make exposure times equal.

Reconsider figure 9(a) to examine the irradiance of the film. The aperture or energy-limiting stop for the system is the circular mask on lens L. The numerical aperture of the spectrograph is small enough to permit all energy passing through the slit to be gathered by the collimating mirror. First, consider the signal obtained when the pivot mirror is rotated to accept energy from the tungsten lamp whose specific intensity is $I_\lambda^{(W)}(T_t)$ where T_t is the true temperature. The solid angle of acceptance as determined by the aperture will be designated Ω_c. The densitometer scanning aperture serves as the field stop and consequently determines how much of the source area is viewed. With lateral magnification m defined as before, the source area viewed is seen to be $W_d H_d / m^2$. Let K_λ be the proportionality constant relating the exposure of the film to deflection of the recording pen. It will be a nonlinear function involving the film characteristic, electronics, and so forth, but is known from sensitometry. Then, the signal $S_{sig}^{(W)}$ is

$$\underset{\text{Deflection}}{S_{sig}^{(W)}} = \underset{\substack{\text{Deflection}\\ \text{per}\\ \text{unit exposure}}}{K_\lambda\left(S_{sig}^{(W)}\right)} \quad \underset{\substack{\text{Optics}\\ \text{transmission}}}{\tau_\lambda^{opt}} \quad \underset{\substack{\text{Wavelength}\\ \text{interval}}}{W_s \frac{d\lambda}{dx}} \quad \underset{\substack{\text{Exposure}\\ \text{time}}}{t^{(W)}} \quad \underset{\substack{\text{Source}\\ \text{area}}}{\frac{W_d H_d}{m^2}} \quad \underset{\substack{\text{Solid}\\ \text{angle}}}{\Omega_c} \quad \underset{\substack{\text{Specific}\\ \text{intensity}}}{I_\lambda^{(W)}(T_t)}$$

It is possible to write τ^{opt} explicitly as the product of all lens transmissions and reflectivities of the system including grating efficiency. This is impractical and unnecessary since, for a T system, the term cancels, as shown subsequently. With the mirror accepting arc radiation and with the addition of a neutral density filter

$$S_{sig}^{(arc)} = K_\lambda\left(S_{sig}^{(arc)}\right)\tau^{opt}\tau^{nd} W_s \frac{d\lambda}{dx} t^{(arc)} \frac{W_d H_d}{m^2} \Omega_c I_\lambda^{(arc)}(T)$$

As previously mentioned, τ^{nd} is adjusted to make $t^{(W)} = t^{(arc)}$. Then

$$I_\lambda^{(arc)} = \frac{S_{sig}^{(arc)}}{S_{sig}^{(W)}} \; \frac{K_\lambda\left(S_{sig}^{(W)}\right)}{K_\lambda\left(S_{sig}^{(arc)}\right)} \; \frac{I_\lambda^{(W)}(T_t)}{\tau_\lambda^{nd}}$$

The specific intensity of the filament is calculated from an observation of its brightness temperature by using a brightness pyrometer having effective wavelength $\lambda_{pyr} = 0.635$ micrometer. The pyrometer is placed for convenience as in figure 9. Then the brightness temperature observed depends on the reflectivity of the mirror $\mathcal{R}$ and T_B is obtained by iterating

$$B_{Str,\lambda_{pyr}}^{o}\left(T_B^{obs}\right) = \mathcal{R}_{\lambda_{pyr}} B_{Str,\lambda_{pyr}}^{o}\left(T_B\right)$$

The true temperature of the lamp is found by using emissivities from Vos (ref. 19) by iterating

$$B^{o}_{Str,\lambda_{pyr}}(T_t) = \epsilon^{(W)}_{\lambda_{pyr}} B^{o}_{Str,\lambda_{pyr}}(T_B)$$

and, finally, the specific intensity at the wavelength of interest by

$$I^{(W)}_{\lambda} = \epsilon^{(W)}_{\lambda} B^{o}_{Str,\lambda}(T_t)$$

This reduction procedure must be repeated for each data point required. Furthermore, in an arc plasma, the line rides on a continuum which can equal it in magnitude. Fortunately, the continuum is nearly constant and its component can be subtracted by using a trace adjacent to the line in question. Since the line intensity result depends on the differences of comparably large numbers and must (unlike the continuum) be corrected for line shape in addition, it loses some of its attractiveness as a temperature indicator. This problem is considered again in the next section. In figure 18 an actual block of raw data is shown with traces and zone boundaries labeled. Barr (ref. 10) has reduced the smoothing and Abel inversion mathematics to a matrix multiplication operation. The measured steradiancy $B_{Str,\lambda}(x)$ is approximated by a discrete data vector whose components are made up of the values taken by $B_{Str,\lambda}$ for equispaced intervals along x. Small segments of this data vector are then fitted with polynomials, substituted into equation (5a) and subsequently integrated term by term. Let Δ be the interval spacing and $I_i = B_{Str,\lambda}(i\Delta)$; then Barr incorporates all of the curve fitting, smoothing, and integration into a matrix $\left(\beta_{ij}\right)$ such that

$$\epsilon_i(r) = \frac{1}{\pi\Delta} \sum_j \beta_{ij} I_j$$

where $\epsilon_i(r) = \epsilon(i\Delta)$, that is, the emission coefficient for the ith radial zone. For a line having transition probability $A_{u\rightarrow l}$, the power per unit volume per steradian is given by

$$\epsilon = \frac{1}{4\pi} N_u A_{u\rightarrow l} h\nu_{lu}$$

where ν_{lu} is the frequency and h is Planck's constant. By using the composition data of table I and the transition probability of reference 16, the emission coefficient has been calculated and is plotted in figure 19. The radial temperature profiles derived by use of 4300 ArI radiation are shown in figure 20.

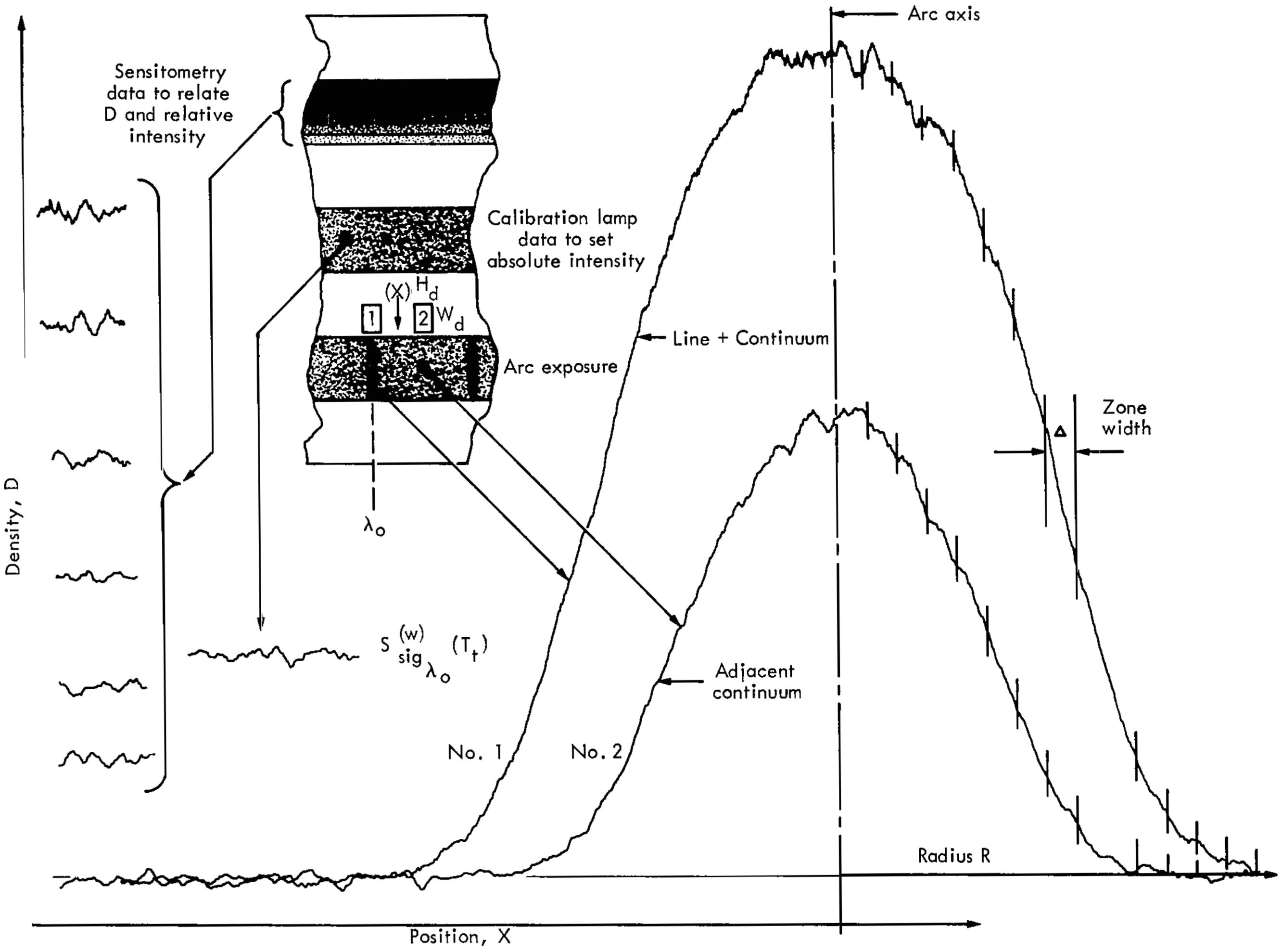

Figure 18.- Sample of data used to obtain emission coefficient for a line and a sketch to show how it is extracted from the plate.

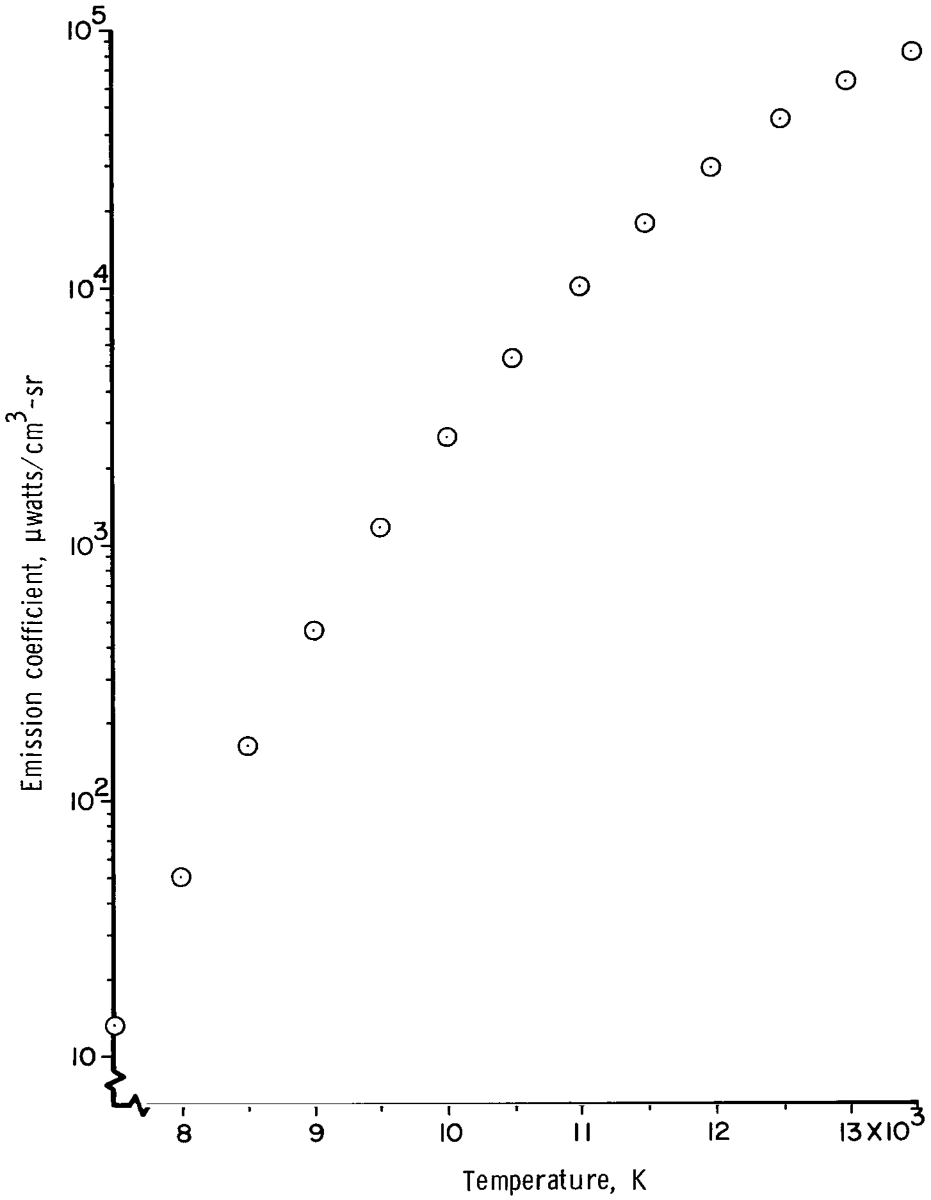

Figure 19.- Variation of emission coefficient with temperature for 4300 ArI.

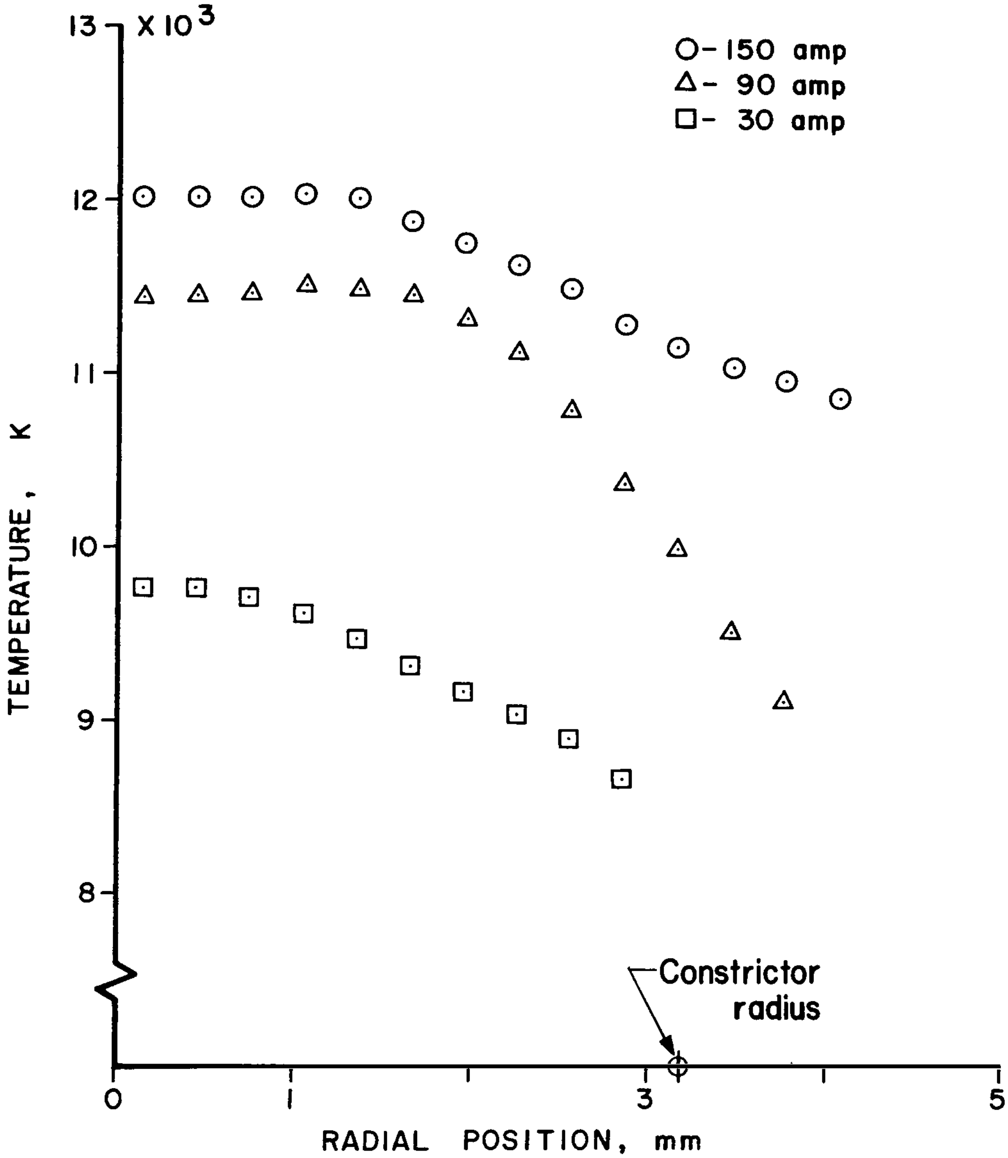

Figure 20.- Temperature profiles for the 30-, 90-, and 150-ampere runs obtained from absolute intensity measurements of 4300 ArI.

All the calculations are done with a machine program so that only certain constants related to the readup need to be entered along with direct deflections from the densitometer traces. In this context, only one comment will be made concerning the analytic form chosen for the film characteristic curve. The conventional plot of density against the logarithm of exposure results in a more or less S-shaped plot referred to as the H and D curve after Hurter and Driffield. This form is an inconvenient one to represent analytically and a recent paper by de Vaucouleurs (ref. 20) redirected attention to a much earlier work by Baker (ref. 21) showing that the "toe" of the curve is considerably straightened by plotting $\log_{10}\left(10^{\mathrm{density}} - 1\right)$ instead of density along the ordinate. For densities of 1 or greater, the curve practically reduces to the original H and D curve, but on the low end considerable linearization occurs. The sensitometry data represented in this way is linear least-squares fitted. The standard output lists the deviations from the fit and thus warns the user of anomalies in the data.

Absolute Continuum Method

Continuum radiation results from free-bound and free-free transitions in the arc plasma. The exact calculation of continuum radiation is only possible for hydrogenic systems. Chapter 5 of reference 1 provides a survey of the working rules for its calculation. Simplified theory predicts the shape of the spectrum very well but leaves the magnitude uncertain by a proportionality factor involving radial overlap integrals called the Gaunt factor, $\xi(\lambda)$. This factor is often taken as a variable and adjusted empirically as is the case for argon. Corliss and Shumaker (ref. 22) provide the expression

$$\epsilon^{\mathrm{cont}} = \frac{9.78 \times 10^{-21} \xi(\lambda)\, N_e^{\,2}}{T^{1/2} \lambda^2 Z_+}, \quad \frac{\mu\mathrm{watts}}{\mathrm{cm}^3\text{-sr-Å}}$$

with λ in angstroms, Z_+ the ion partition function, and $\xi(4315\ \text{Å}) = 2.3$. This expression is used to calculate the last column in table I which is plotted in figure 21. The temperature profiles derived from continuum intensity measurements are shown in figure 22. The continuum measurements have the advantage over line measurements in that no line shape or background corrections need to be made.

Electron Density Method

The electron density N_e is a unique function of temperature in an equilibrium calculation. This quantity may be used along with table I to ascertain the temperature. The shift and broadening of spectral lines are functions of the local electron density. In figure 23 is shown the argon spectrum at 30 and 150 amperes bracketed by an iron (Fe) reference. The shift and broadening of the high current spectrum is readily apparent as

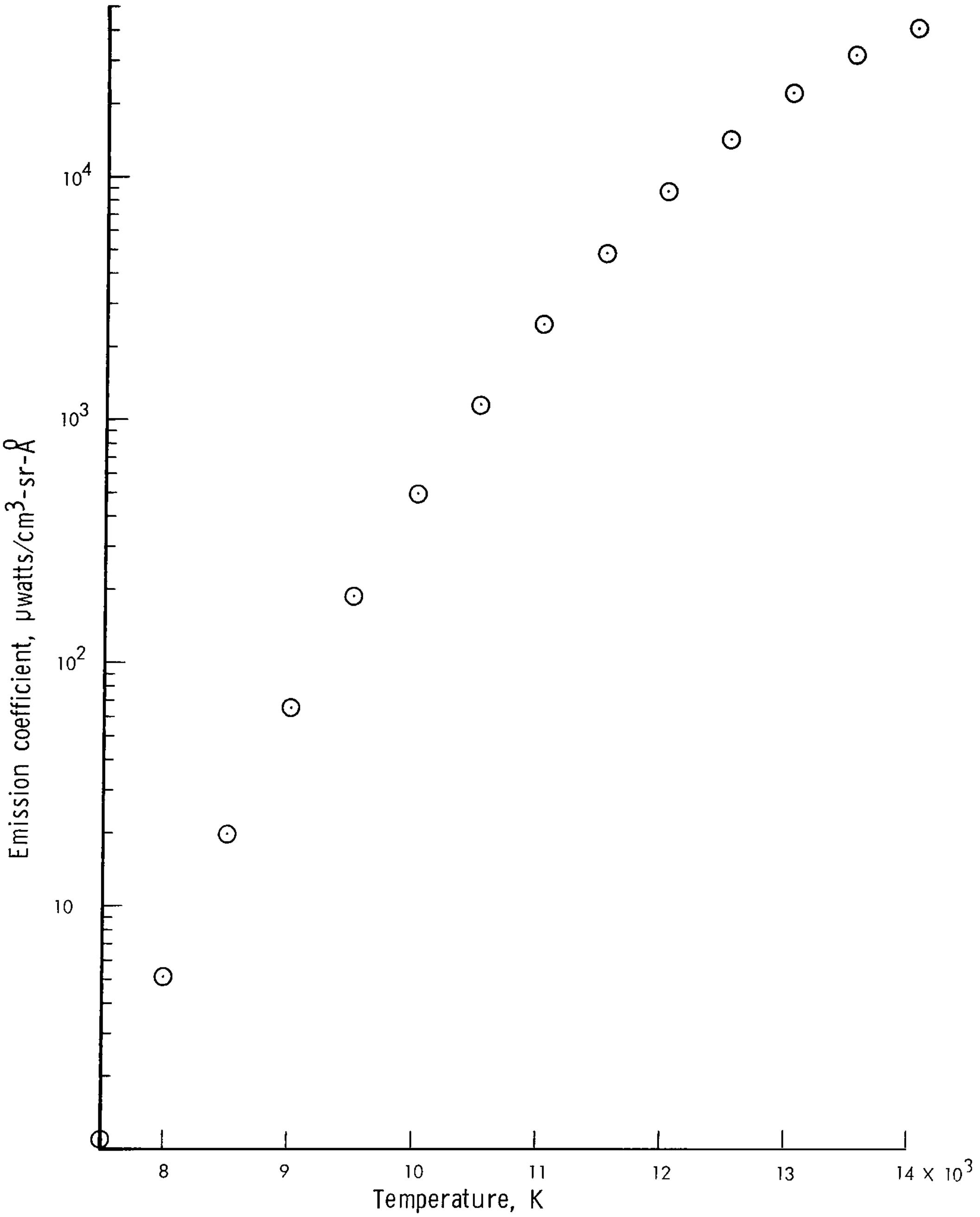

Figure 21.- Variation of emission coefficient with temperature for 1 angstrom swath of continuum at 4315 angstroms.

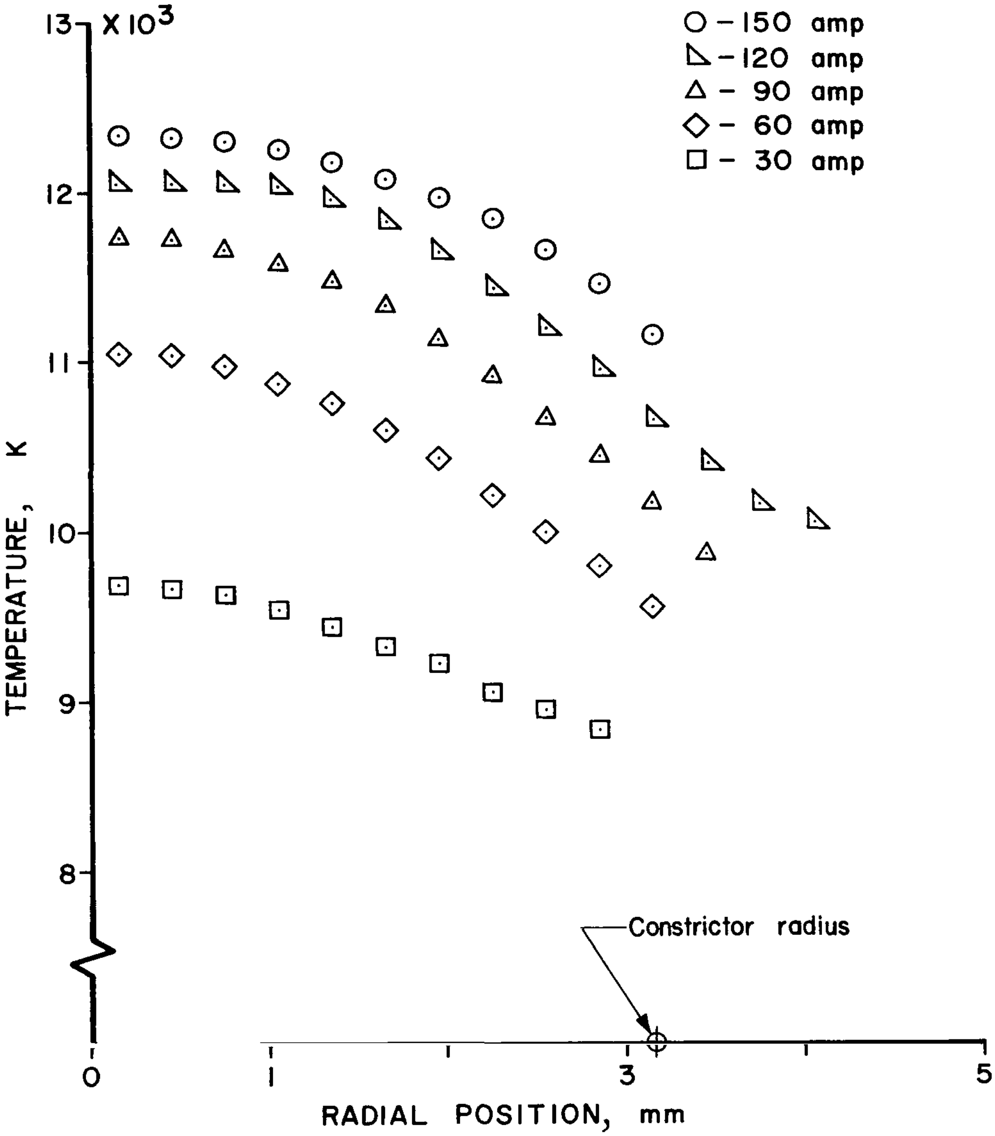

Figure 22.- Temperature profiles obtained from absolute continuum intensity at 4315 angstroms.

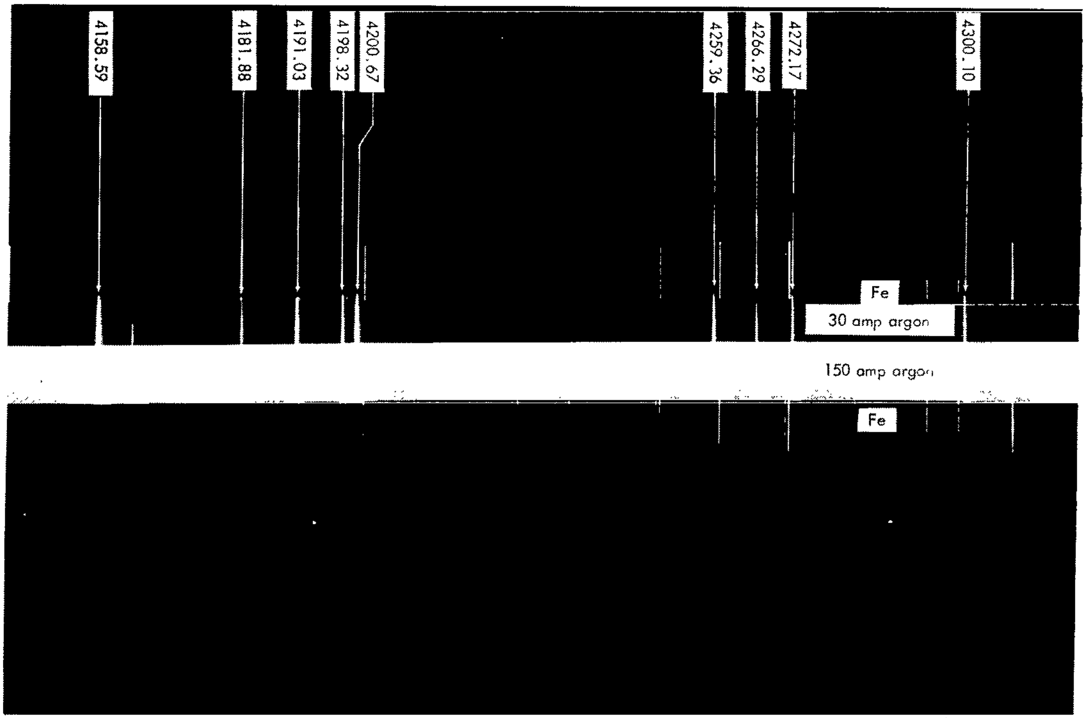

L-72-124

Figure 23.- 30- and 150-ampere runs to illustrate enhanced continuum, line shift, and line breadth at high electron density.

is the increased continuum contribution which goes as N_e^2. The high-amperage case has been exposed slightly longer to enhance the asymmetry. Although some approximate calculations of shift d and full width at half peak w are tabulated (for example, ref. 1), again the safest procedure is to use empirical results obtained by performing experiments with traces of hydrogen added whose line shapes are very reliable and serve to determine the local electron density. Popenoe and Shumaker (ref. 16) have used this approach to determine constants pertinent to 4300 ArI and find

$$w = 0.2 \times 10^{-16} N_e (\text{Å})$$

and

$$d = 0.103 \times 10^{-16} N_e (\text{Å})$$

with N_e in cm^{-3}.

To avoid problems with unfolding line profiles, the arc is viewed axially and only the central zone is measured. The slits are set to diffraction fill the collimator. This setting results in an essentially Gaussian apparatus function having a full width of 0.016 angstrom. The narrowest full width at half peak measured was on the order of 0.2 angstrom which is more than 4 times the spectral slit width of the spectrograph having a 10^{-2}-mm (10-micron) entrance slit. Kostkowski and Bass (ref. 23, fig. 2) plot the relative width error encountered because of apparatus broadening as a function of the ratio of spectral width to true width. From this curve, the largest expected error encountered in this experiment should be less than 2 percent and is neglected.

Axial temperatures measured by use of Stark results are compared with those derived from other measurements in figure 24. The lines are very broad and the peaks are difficult to determine; thus, the shifts are difficult to measure accurately. The width measurement is a little easier to do. Agreement seems adequate in view of the fact that formulas provided by Griem (ref. 1) for the same line differ from these values by 20 or 30 percent.

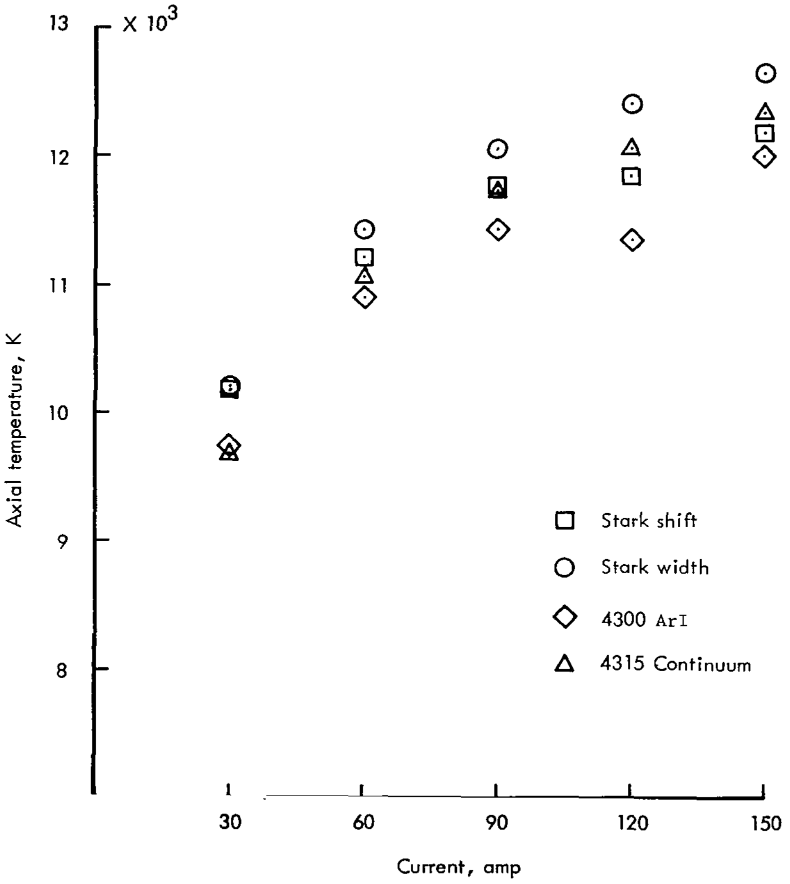

Figure 24.- Comparison of axial temperatures ascertained by different techniques.

CONCLUSIONS

The Abel integral relationship for inverting "side on" spectroscopic data is seen to follow from assuming cylindrical symmetry, optical thinness, and nonconverging optics. Its restriction to sources which have a finite extent is seen to follow from the boundary conditions imposed on the explicit solution of the integral equation for the transform partner. From the analysis the following conclusions are made:

1. The dimensions of the scanning aperture on the densitometer and the aperture stop on the lens which images the source onto the spectrograph slit combine to determine the spatial resolution obtainable with the Abel inversion.

2. There will always be some underestimation of the emission coefficient derived from inverted data because of converging optics but this value can be kept small by appropriate choice of stops and optical component spacings.

3. Approximate theoretical estimates of optical depth are risky and it is best to rely on empirical determinations if the source geometry allows for it.

4. Absolute intensities for highly broadened lines require correction due to background and line shape; thus, absolute continuum measurements are made more attractive for temperature determination when empirical Gaunt factors exist.

5. Stark width and shift temperature measurements operate indirectly through the electron density, are difficult to acquire especially in the nonhomogeneous case, and except for hydrogenic systems are hard to interpret because of discrepancies in the literature.

Langley Research Center,
National Aeronautics and Space Administration,
Hampton, Va., February 9, 1972.

APPENDIX A

DEPTH OF FIELD FOR A SINGLE LENS

Although most people have an intuitive feeling for depth of field, it is surprisingly difficult to come by its discussion in optics books and even more so to find a working formula for it. Consider figure 25 which depicts an ideal thin lens L having focal length F and aperture D. This lens will image an axial point at S into S'. The depth of focus concept is introduced as follows: If the plane of observation were moved by $\delta/2$ toward or away from the lens, the spot of diameter ϵ would still be an acceptable image of the point. As with any discussion of resolution, the criterion of acceptability has an element of arbitrariness, but, in practice, it could be the minimum dimension resolvable by a particular film as stated in the manufacturer's specifications.

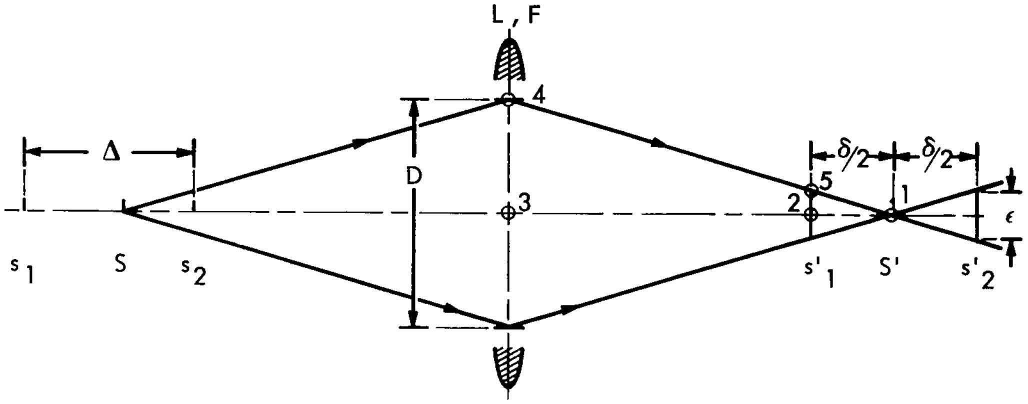

Figure 25.- Single lens depth of field diagram.

By using similar triangles 125 and 134 (fig. 25),

$$\frac{D/2}{S'} = \frac{\epsilon/2}{\delta/2}$$

or

$$\delta = \frac{2S'\epsilon}{D} \qquad \text{(Depth of focus)} \qquad \text{(A1)}$$

All axial points between s_1 and s_2 conjugate to s_1' and s_2', respectively, will satisfy the criterion of acceptability and, in fact, $s_1 - s_2 \equiv \Delta$ will be termed the depth of field. Since $s_1' = S' - \frac{\delta}{2}$ and $s_2' = S' + \frac{\delta}{2}$, the Gaussian equations pertinent to the thin lens read

$$\frac{1}{S' + \frac{\delta}{2}} + \frac{1}{s_2} = \frac{1}{F} \tag{A2a}$$

$$\frac{1}{S' - \frac{\delta}{2}} + \frac{1}{s_1} = \frac{1}{F} \tag{A2b}$$

Equating the left-hand sides of these equations yields

$$\frac{1}{S' + \frac{\delta}{2}} + \frac{1}{s_2} = \frac{1}{S' - \frac{\delta}{2}} + \frac{1}{s_1}$$

and rearranging yields

$$\frac{1}{s_2} - \frac{1}{s_1} = \frac{1}{S' - \frac{\delta}{2}} - \frac{1}{S' + \frac{\delta}{2}}$$

By using the least common denominators and the definition of depth of field Δ,

$$\Delta = \frac{\delta}{S'^2 - \frac{\delta^2}{4}} s_1 s_2 \tag{A3a}$$

$$\Delta = \frac{\delta}{S'^2\left(1 - \frac{\epsilon^2}{D^2}\right)} s_1 s_2 \tag{A3b}$$

In practice, $(\epsilon/D)^2 << 1$ and can be neglected. Then,

$$\Delta \approx \frac{\delta}{S'^2} s_1 s_2 \tag{A3c}$$

If $s_1 \approx s_2 \approx S$,

$$\Delta \approx \frac{\delta}{m^2} = \frac{2S'\epsilon}{m^2 D} \tag{A3d}$$

where m is the linear magnification, $-\frac{S'}{S}$, and its square is usually referred to as longitudinal magnification.

Although this final form is concise and useful, it should be remembered that it is essentially a differential approximation and if Δ becomes, for example, 10 percent of S, it is advisable to use the relations (A3c) and (A3b) with s_1 and s_2 substituted from equation (A2).

REFERENCES

1. Griem, Hans R.: Plasma Spectroscopy. McGraw-Hill Book Co., Inc., c.1964.
2. Knopp, Carl F.: An Experimental Determination of the Thermal and Electrical Conductivity of Atmospheric Argon Plasma. NU-GDL Rep. B-1-65 (Contract AFOSR 49(638)-879), Northwestern Univ. Technol. Inst., Jan. 1965. (Available from DDC as AD 621 213.)
3. Emmons, Howard W.: Arc Measurement of High-Temperature Gas Transport Properties. Phys. Fluids, vol. 10, no. 6, June 1967, pp. 1125-1136.
4. Bott, J. F.: Spectroscopic Measurement of Temperatures in an Argon Plasma Arc. Phys. Fluids, vol. 9, no. 8, Aug. 1966, pp. 1540-1547.
5. Sheyndlin, A. Ye.; and Asinovskiy, E. I.: Investigations of the Electrical and Optical Properties of Argon in a Stabilized Arc. FTD-TT-65-1236/1+2, U.S. Air Force, Dec. 1965.
6. Shumaker, John B., Jr.: Arc Source for High Temperature Gas Studies. Rev. Sci. Instrum., vol. 32, no. 1, Jan. 1961, pp. 65-67.
7. Finkelnburg, W.; and Maecker, H.: Elektrische Bögen und thermisches Plasma. Handbuch d. Physik, Bd. XXII, Springer-Verlag, 1956, pp. 254-444.
8. Wiese, W. L.; Paquette, D. R.; and Solarski, J. E.: Profiles of Stark-Broadened Balmer Lines in a Hydrogen Plasma. Phys. Rev., vol. 129, no. 3, Feb. 1, 1963, pp. 1225-1232.
9. Dwight, Herbert Bristol: Tables of Integrals and Other Mathematical Data. Fourth ed., Macmillan Co., 1961.
10. Barr, William L.: Method for Computing the Radial Distribution of Emitters in a Cylindrical Source. J. Opt. Soc. Amer., vol. 52, no. 8, Aug. 1962, pp. 885-888.
11. Bockasten, Kjell: Transformation of Observed Radiances Into Radial Distribution of the Emission of a Plasma. J. Opt. Soc. Amer., vol. 51, no. 9, Sept. 1961, pp. 943-947.
12. Welford, W. T.: Geometrical Optics – Optical Instrumentation. North-Holland Pub. Co., 1962.
13. Burington, Richard Stevens: Handbook of Mathematical Tables and Formulas. Third ed., Handbook Publishers, Inc., 1949.
14. Cowley, Charles R.: The Theory of Stellar Spectra. Gordon & Breach, Sci. Publ., Inc., c.1970.

15. Penner, S. S.: Quantitative Molecular Spectroscopy and Gas Emissivities. Addison-Wesley Pub. Co., Inc., c.1959.

16. Popenoe, C. H.; and Shumaker, J. B., Jr.: Arc Measurement of Some Argon Transition Probabilities. J. Res. Nat. Bur. Stand., A, vol. 69A, no. 6, Nov.-Dec. 1965, pp. 495-509.

17. Dickerman, Philip J., ed.: Optical Spectrometric Measurements of High Temperatures. Univ. Chicago Press, c.1961.

18. Wiese, W. L.; Smith, M. W.; and Glennon, B. M.: Atomic Transition Probabilities. Vol. I – Hydrogen Through Neon. NSRDS-NBS 4, U.S. Dep. Com., May 20, 1966.

19. de Vos, J. C.: A New Determination of the Emissivity of Tungsten Ribbon. Physica. vol. 20, no. 10, Oct. 1954, pp. 690-714.

20. de Vaucouleurs, Gerard: Linearization of Characteristic Curves in Photographic Photometry. Appl. Opt., vol. 7, no. 8, Aug. 1968, pp. 1513-1518.

21. Baker, E. A.: Blackening of Photographic Plates at Low Densities. Proc. Roy. Soc. Edinburgh, vol. 45, no. 2, 1924-1925, pp. 166-186.

22. Corliss, C. H.; and Shumaker, J. B., Jr.: Transition Probabilities in Argon I. J. Res. Nat. Bur. Stand., A, vol. 71A, no. 6, Nov.-Dec. 1967, pp. 575-581.

23. Kostkowski, Henry J.; and Bass, Arnold M.: Slit Function Effects in the Direct Measurement of Absorption Line Half-Widths and Intensities. J. Opt. Soc. Amer., vol. 46, no. 12, Dec. 1956, pp. 1060-1064.

TABLE I.- TEMPERATURE DEPENDENCE OF QUANTITIES ENTERING INTO THE SPECTROSCOPIC MEASUREMENT

[Composition data and spectroscopic constants from reference 16.
4300 ArI: $A = 4.11 \times 10^{5}\ \text{sec}^{-1}$ (±11%)
$g_u = 5$; $E_u = 116999.4\ \text{cm}^{-1}$;
$g_l = 3$; $E_l = 93750.6\ \text{cm}^{-1}$.]

Temperature, K	N_e, cm^{-3}	N_l, cm^{-3}	N_u, cm^{-3}	a	ϵ^{L}, $\frac{\mu\text{watts}}{\text{cm}^3\text{-sr}}$ (a)	ϵ^{cont}, $\frac{\mu\text{watts}}{\text{cm}^3\text{-sr-Å}}$ (b)
7 500	6.684×10^{14}	4.540×10^{10}	8.755×10^{8}		1.324×10^{1}	1.100×10^{0}
8 000	1.453×10^{15}	1.307×10^{11}	3.331×10^{9}	0.5	5.037×10^{1}	5.100×10^{0}
8 500	2.898×10^{15}	3.305×10^{11}	1.077×10^{10}		1.628×10^{2}	1.980×10^{1}
9 000	5.352×10^{15}	7.490×10^{11}	3.037×10^{10}		4.592×10^{2}	6.520×10^{1}
9 500	9.254×10^{15}	1.544×10^{12}	7.614×10^{10}		1.151×10^{3}	1.892×10^{2}
10 000	1.511×10^{16}	2.930×10^{12}	1.723×10^{11}	5.6	2.605×10^{3}	4.901×10^{2}
10 500	2.342×10^{16}	5.163×10^{12}	3.560×10^{11}		5.383×10^{3}	1.146×10^{3}
11 000	3.466×10^{16}	8.488×10^{12}	6.764×10^{11}		1.023×10^{4}	2.446×10^{3}
11 500	4.910×10^{16}	1.307×10^{13}	1.189×10^{12}		1.798×10^{4}	4.789×10^{3}
12 000	6.672×10^{16}	1.887×10^{13}	1.937×10^{12}	23.7	2.929×10^{4}	8.636×10^{3}
12 500	8.705×10^{16}	2.556×10^{13}	2.934×10^{12}		4.436×10^{4}	1.438×10^{4}
13 000	1.091×10^{17}	3.249×10^{13}	4.133×10^{12}		6.249×10^{4}	2.210×10^{4}
13 500	1.315×10^{17}	3.871×10^{13}	5.417×10^{12}		8.191×10^{4}	3.145×10^{4}
14 000	1.525×10^{17}	4.328×10^{13}	6.616×10^{12}	53.2	1.000×10^{5}	4.147×10^{4}

[a] Emission coefficient for 4300 ArI.

[b] Continuum emission coefficient at 4315 angstroms using the formula of reference 22.

NATIONAL AERONAUTICS AND SPACE ADMISTRATION
WASHINGTON, D.C. 20546

OFFICIAL BUSINESS
PENALTY FOR PRIVATE USE $300

FIRST CLASS MAIL

027 001 C1 U 25 720317 S00903DS
DEPT OF THE AIR FORCE
AF WEAPONS LAB (AFSC)
TECH LIBRARY/WLOL/
ATTN: E LOU BOWMAN, CHIEF
KIRTLAND AFB NM 87117

> *"The aeronautical and space activities of the United States shall be conducted so as to contribute . . . to the expansion of human knowledge of phenomena in the atmosphere and space. The Administration shall provide for the widest practicable and appropriate dissemination of information concerning its activities and the results thereof."*
>
> —NATIONAL AERONAUTICS AND SPACE ACT OF 1958

NASA SCIENTIFIC AND TECHNICAL PUBLICATIONS

TECHNICAL REPORTS: Scientific and technical information considered important, complete, and a lasting contribution to existing knowledge.

TECHNICAL NOTES: Information less broad in scope but nevertheless of importance as a contribution to existing knowledge.

TECHNICAL MEMORANDUMS: Information receiving limited distribution because of preliminary data, security classification, or other reasons.

CONTRACTOR REPORTS: Scientific and technical information generated under a NASA contract or grant and considered an important contribution to existing knowledge.

TECHNICAL TRANSLATIONS: Information published in a foreign language considered to merit NASA distribution in English.

SPECIAL PUBLICATIONS: Information derived from or of value to NASA activities. Publications include conference proceedings, monographs, data compilations, handbooks, sourcebooks, and special bibliographies.

TECHNOLOGY UTILIZATION PUBLICATIONS: Information on technology used by NASA that may be of particular interest in commercial and other non-aerospace applications. Publications include Tech Briefs, Technology Utilization Reports and Technology Surveys.

Details on the availability of these publications may be obtained from:

SCIENTIFIC AND TECHNICAL INFORMATION OFFICE

NATIONAL AERONAUTICS AND SPACE ADMINISTRATION
Washington, D.C. 20546